Determination of the vertical distribution of in-cloud particle shape using ~~SLDR~~ SLDR mode 35-GHz scanning cloud radar

Audrey Teisseire[1], Patric Seifert[1], Alexander Myagkov[2], Johannes Bühl[1], and Martin Radenz[1]

[1]Leibniz Institute for Tropospheric Research, Permoserstraße 15, 04318 Leipzig, Germany
[2]RPG Radiometer Physics GmbH, Werner-von-Siemens-Str. 4, 53340 Meckenheim, Germany

Correspondence: Audrey Teisseire (teisseire@tropos.de)

Abstract. In this study we present an approach that uses ~~polarimetric variables~~ the polarimetric variable SLDR (Slanted Linear Depolarization Ratio) from a scanning polarimetric cloud radar MIRA-35 in the ~~45° slanted linear depolarization (SLDR)~~ SLDR configuration, to derive the vertical distribution of particle shape (VDPS) between top and base of mixed-phase cloud systems. The polarimetric parameter ~~SLDR~~ SLDR was selected for this study due to its strong sensitivity to shape and low sensitivity to the wobbling effect of particles at different antenna elevation angles. For the VDPS method, elevation scans from 90° to 30° elevation angle were deployed to estimate the vertical profile of the particle shape by means of the polarizability ratio, which is a measure of the density-weighted axis ratio. Results were obtained by retrieving the best fit between observed ~~SLDR-vs-elevation dependencies~~ SLDR from 90° to 30° elevation angle and respective values simulated with a ~~spheroid~~ spheroidal scattering model. The applicability of the new method is demonstrated by means of three case studies of isometric, columnar and ~~oblate~~ plate-like hydrometeor shapes, respectively, which were obtained from measurements at the Mediterranean site of Limassol, Cyprus. The identified hydrometeor shapes are demonstrated to fit well to the cloud and thermodynamic conditions which prevailed at the times of observations. ~~Some observations reveal that in mixed-phased clouds~~ A fourth case study demonstrates a scenario where ice particle shapes tend to evolve from a pristine ~~columnar or dendritic~~ state at cloud top toward a more isometric shape or less dense particles at cloud base. Either aggregation or riming processes contribute to this vertical change of microphysical properties. The new height-resolved identification of hydrometeor shape and the potential of the VDPS method to derive its vertical distribution are helpful tools to understand complex processes such as riming or aggregation, which occur particularly in mixed-phase clouds.

1 Introduction

In the troposphere, a rich variety of cloud types exists, which are formed by characteristic microphysical processes. The structure of clouds is in general determined by the complex interaction of water vapor, ice, liquid droplets, vertical air motion and aerosol particles, acting as cloud condensation nuclei (CCN) or ice nucleating particles (INP) ~~(Morrison et al., 2012; Ansmann et al., 2019)~~ (Pruppacher and Klett, 1997; Morrison et al., 2012; Ansmann et al., 2019). While in warm clouds the collision-coalescence process is the primary process responsible for the formation of precipitation, the situation is more complicated in ice-containing clouds having temperatures between -40°C and 0°C. In this temperature range, the coexistence of supercooled liquid water and ice is possible. Thus, in these mixed-phase clouds, multiple cloud microphysical processes are intertwined as they contain a three-phase colloidal system consisting of water vapor, ice particles and supercooled liquid droplets (Korolev et al., 2017). The initial partitioning between the ice and liquid water is determined by the CCN and INP reservoir and represents the prevalent conditions for secondary ice formation processes, riming and aggregation (Solomon et al., 2018; Fan et al., 2017), which are greatly involved in the precipitation transition in mixed-phase clouds.

Observation of the hydrometeor habit is a possible way to study cloud formation and precipitation because particle shape can be considered a fingerprint of crucial processes, including crystal growth, evaporation rate, ice crystal fall speed, and cloud radiative properties (e.g., Avramov and Harrington, 2010). Shape allows to distinguish pristine ice crystals from hydrometeors which have grown via aggregation or riming processes and can be considered as a tracer of the different processes contributing to the evolution of a cloud system. The overall structure of ice crystals grown in air can be classified into plate-like and columnar shapes as a function of temperature between $-40°$ and $0°$C. Bühl et al. (2016) and Myagkov et al. (2016a) showed that primary ice formation dominates in thin layers of stratiform or mixed-phase clouds of a geometrical thickness $\leq 350\,\mathrm{m}$, as growth processes in these thin clouds are constrained (Fukuta and Takahashi, 1999). In such cloud systems and conditions of liquid water saturation, the shape of ice crystals is thus related directly to the environmental temperature (Myagkov et al., 2016b). However, further complexity can be expected when the cloud systems become deeper and when the thermodynamic structure is less well defined as in single-layer stratiform mixed-phase clouds. Techniques which allow detecting the hydrometeor shape have high potential to contribute additional capabilities for the monitoring of cloud systems, to expand the understanding of the involved microphysical properties, and to support the improvement of the representation of these processes in numerical models. A way to discriminate different hydrometeor populations is the separation of peaks in cloud radar Doppler spectra (Radenz et al., 2019; Kalesse et al., 2019) (Radenz et al., 2019; Kalesse et al., 2019; Luke et al., 2021) using observations of ground-based cloud radar. However, this technique is limited, e.g., with respect to atmospheric turbulence, which broadens the spectra and makes the detection and separation of peaks difficult or even impossible. Moreover, hydrometeors with similar terminal fall velocities (for example drizzle and small ice) cannot be distinguished in the Doppler spectrum. In this case, it is possible to have a look at the Doppler spectra of polarimetric parameters such as LDR or SLDR to confirm in which spectral mode the crystals are present.

Polarimetric cloud radar techniques have been shown to be valuable tools for the qualitative detection of ice crystal shape (Matrosov et al., 2001; Reinking et al., 2002; Matrosov et al., 2005). Matrosov et al. (2012) demonstrated an approach where they associated measurements of Slanted Linear Depolarization Ratio (SLDR) mode scanning cloud radar to visual observations of ice crystal habits during a precipitation event. While this their study demonstrates well the relationship between SLDR SLDR signatures and particle shape, it did not yet allow to quantify the particle shape directly based on the measurements. Such an approach has been presented by Myagkov et al. (2016a), who succeeded in predicting the particle shape and orientation based on hybrid-mode scanning cloud radar observations by means of the two quantitative parameters polarizability ratio and degree of orientation, respectively. Myagkov et al. (2016a) have shown that existing backscattering models, assuming the spheroidal approximation of cloud scatters, can be applied to establish a link between a set of measured polarimetric variables and the polarizability ratio. Polarizability ratio is a parameter defined by the geometric aspect ratio of particles and their refractive index. For ice particles the refractive index is almost a linear function of their apparent ice density. Note, that it is not directly possible to infer the aspect ratio and the apparent ice density from the polarizability ratio. However, since the polarizability ratio depends on ~~the aspect ratio and the apparent ice density~~both variables, we suggest using it to track the evolution of the ice particles from pristine state to aggregates and rimed particles. Even though developed for ~~SLDR~~ SLDR mode and Simultaneous Transmit Simultaneous Receive (STSR, hybrid)-mode cloud radars, applicability of the shape and orientation estimation retrieval was originally demonstrated only for a STSR-mode scanning 35-GHz cloud radar, based on observations of stratiform cloud layers during the one-month field campaign Analysis of Composition of Clouds with Extended Polarization Techniques (ACCEPT, Myagkov et al. (2016a)).

~~The~~ Even though the number of scanning STSR-mode cloud radars has been continuously growing in Europe, a number of measurement sites within ACTRIS (the Aerosol, Clouds and Trace Gases Research Infrastructure) are equipped with scanning LDR radars (Madonna et al., 2013; Löhnert et al., 2015; Tetoni et al., 2022). Such radars can be modified to the SLDR mode with relatively low efforts and investments, and as a result can provide long-term observational datasets for retrieving the polarizability ratio of ice-containing clouds in different climatic zones. Therefore, the main goal of this study is to derive the vertical distribution of particle shape in clouds using the ~~spheroid~~ spheroidal scattering model developed by Myagkov et al. (2016a) for application to regular long-term observations of a SLDR-mode 35-GHz scanning cloud radar. We introduce a simplified and versatile version of the original STSR-mode approach by concentrating on the retrieval of the polarizability ratio, as we consider this parameter to be more relevant for the investigation of cloud microphysical processes in comparison to the degree of orientation. ~~By doing so, observations of SLDR are sufficient for the retrieval, enabling a broader field of application.~~ This paper aims on demonstrating the ability of ~~this new method, herafter referred to~~ the Vertical Distribution of Particle Shape (VDPS) method, to ~~derive particle shape~~ characterize particle properties using data with a newly configured SLDR-mode 35-GHz cloud radar which was deployed in the Cyprus Clouds, Aerosols and pRecipitation Experiment (CyCARE, Ansmann et al. (2019)) field campaign ~~located~~ in Limassol, Cyprus. We also illustrate that a profile of the derived polarizability ratio can be potentially used to detect microphysical processes affecting the evolution of ice particles in deep precipitating clouds. In Section 2, instrumentation~~and campaign setup~~, campaign setup and the polarimetric parameter SLDR will be described~~and the~~. The VDPS method will be introduced in Section 3 ~~. An evaluation~~ and an evaluation of the VDPS method is presented in Section 4~~, where case~~. Case studies showing isometric particles, columnar crystals and~~dendrites, respectively,~~ , plate-like crystals will be discussed, and a fourth case study showing a transformation in shape of particles from cloud top to cloud base will be presented to demonstrate the potential of the VDPS method to detect and describe microphysical transformation processes. In Section 5, we will elaborate on the advantages and limits of this new algorithm as well as on possible future improvements.

Table 1. Technical characteristics of MIRA-35 SLDR-mode cloud radar during the deployment in the CyCARE campaign in Limassol, Cyprus.

Parameters	Values
Pulse power	30 kW
Pulse length	208 ns
Pulse repetition frequency	7500 Hz
Elevation angle velocity	0.5 deg.s^{-1}
nFFT points	512
Number of range gates	498
Number of spectral averages	15
Integration time	1 s
Range resolution	31.18 m
Reflectivity sensitivity	-48 dBZ
co-cross-channel isolation	-35 dB

2 Dataset

2.1 ~~SLDR-mode~~ SLDR mode 35-GHz cloud radar MIRA-35

The central instrument for the present study is a modified version of the 35-GHz cloud radar Mira-35, which is operated in ~~SLDR-mode~~SLDR mode. MIRA-35 in general is a dual-polarization (LDR-mode) radar which emits linearly polarized radiation through the co-channel, while the returned signals are received in both the co- and cross-channels. The ~~SLDR-mode~~ SLDR mode cloud radar was implemented based on the conventional Linear Depolarization Ratio (LDR) ~~-mode~~ mode by 45° rotation of the antenna system around the emission direction. While numerous polarimetric configurations of radar systems exist (Bringi and Chandrasekar, 2001, Ch. 6), the LDR mode is currently the most common one amongst cloud radars. The properties of the standard LDR mode Mira-35 are elaborated in detail in Görsdorf et al. (2015). The technical characteristics of MIRA-35 used in the CyCARE campaign in Limassol, Cyprus, are ~~detailed~~ given in the Table 1. Standard vertical-stare LDR-mode allows only to discriminate between hydrometeors with an isometric intersection and with a columnar intersection (Bühl et al., 2016). I.e., aggregates cannot be separated from generally horizontally oriented ~~dendritic~~ plate-like particles in vertical-stare mode because their scattering intersections appear to be similar. In order to optimize the Mira-35 cloud radar for improved measurements of hydrometeor shape and orientation, two modifications were applied to the standard setup as it is described by Görsdorf et al. (2015). First, the cloud radar was mounted onto a positioner platform which allows for a freely definable position of the radar within a half sphere given by 360° of azimuth and 180° of elevation. The second modification addresses a 45° rotation of the receiver antenna around the emission direction. This operation mode, in general defined as ~~SLDR-mode~~SLDR mode, has specific advantages in studies of the intrinsic relationship between the polarimetric signature of

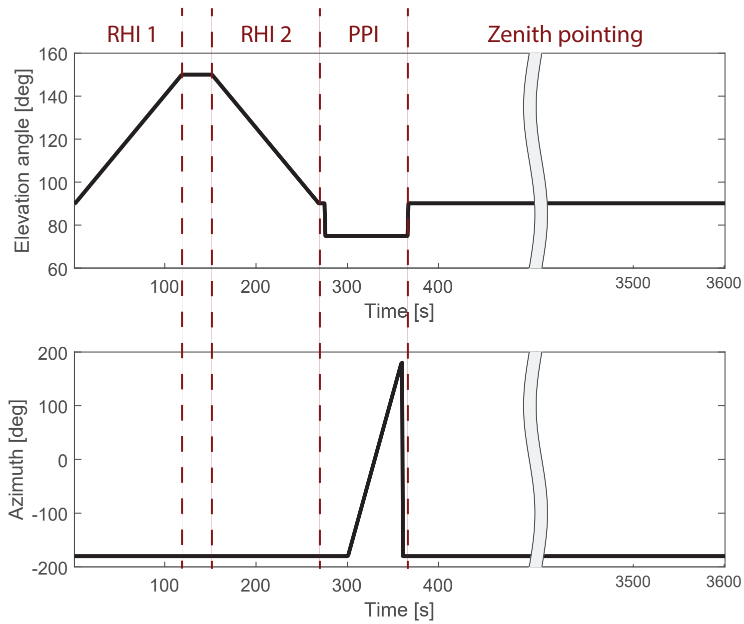

Figure 1. ~~Depiction of the temporal~~ Temporal evolution of elevation angle (top) and ~~azmith~~ azimuth angle (bottom) during the hourly scan cycle of ~~SLDR~~ SLDR Mira-35 as applied during CyCARE. Red-colored dashed vertical lines denote the time periods of the different RHI (range-height indicator)~~and~~ , PPI (~~plane-position~~ plan-position indicator) and zenith-pointing scan patterns.

the particle shape and radar elevation angle. In contrast to the standard LDR mode, variations in the orientation of hydrometeors only have small effects on the measured ~~SLDR (δ_s)~~SLDR, even at low elevation angles (Matrosov, 1991). In turn, ~~δ_s~~ SLDR in vertical pointing mode (elevation = 90°) is similar to the LDR observed with standard Mira-35 systems. This behavior is also of advantage because it ensures direct comparability to other standard LDR-mode radars in vertical-pointing measurements. In the framework of the presented study, the radar was steered toward geographic south direction (180° azimuth angle) and performed range-height-indicator (RHI) scans from 90° (~~zenith pointing~~zenith-pointing) to 150°, corresponding to 30° elevation over the horizon toward north direction. This notation of the elevation angle range will be used throughout this article and ~~on the figure captions~~figures.

Figure 1 describes the setup of one scan cycle as it was applied in the measurements of the ~~SLDR-mode~~ SLDR mode MIRA-35, used in this study. Each scan cycle starts at minute 29 of each hour. Within 6.5 minutes, two ~~RHI-scans~~ RHI scans from 90° to 150° and from 150° to 90° elevation angle and one Plan Position Indicator (PPI) scan at 75° elevation are performed. During the remaining 53.5 minutes of each measurement hour, vertical-stare observations (at 90° elevation angle) are performed to support standard retrievals, such as done within Cloudnet (Illingworth et al., 2007; Radenz et al., 2021) or as required for Doppler-spectra analysis techniques (Radenz et al., 2019; Bühl et al., 2019; Vogl et al., 2022; Schimmel et al., 2022). A limit of 150° elevation angle was established to avoid physical barriers like trees or buildings. It is also a reasonable compromise between required horizontal homogeneity and the intensity of the SLDR SLDR gradient produced by the observed hydrometeors. As the detailed procedure of data acquisition was depicted by Görsdorf et al. (2015) and Myagkov et al. (2016b), the determination of the polarimetric parameters required for this study is only briefly outlined below. The primary measurement parameters are thus the complex Doppler Doppler power spectra received by the detectors in the co- and cross-channel cross-channels with respect to the emitted polarization plane $\dot{S}_{\mathrm{co}}(\omega_k)$ and $\dot{S}_{\mathrm{cx}}(\omega_k)$ $P_{\mathrm{co}}(\omega_k)$ and $P_{\mathrm{cx}}(\omega_k)$, respectively, with ω_k being the Doppler frequency shift of each individual spectral component k. The herein presented VDPS method only considers the main peak of the detected Doppler spectrum in the co-channel. Thus, in a next step, each data point is screened for the spectral component $\omega_k^{\max}$ where $\dot{S}_{\mathrm{cx}}(\omega_k)$ $P_{\mathrm{co}}(\omega_k)$ is maximal. The following parameters are parameter is then only calculated for the Doppler spectral bin $\omega_k^{\max}$. The frequency dependency is thus omitted in the following and the polarimetric properties linear depolarization ratio SLDR (δ_{s}) and co-cross-correlation coefficient (ρ_{s}) in slanted mode (SLDR) can be derived as follows:

$$\delta_s \mathrm{SLDR} = \frac{\dot{\mathrm{S}}_{\mathrm{cx}}\dot{\mathrm{S}}^*_{\mathrm{cx}}}{\dot{\mathrm{S}}_{\mathrm{co}}\dot{\mathrm{S}}^*_{\mathrm{co}}} \frac{\langle \mathrm{P}_{\mathrm{cx}} \rangle}{\langle \mathrm{P}_{\mathrm{co}} \rangle} \tag{1}$$

$$\rho_s = \frac{|\langle \dot{S}_{\mathrm{co}} \dot{S}_{\mathrm{cx}} \rangle|}{\left(\langle \dot{S}_{\mathrm{co}} \dot{S}^*_{\mathrm{co}} \rangle \langle \dot{S}_{\mathrm{cx}} \dot{S}^*_{\mathrm{cx}} \rangle\right)^{1/2}}.$$

where $*$ is the complex conjugateWhere $\langle\rangle$ denotes averaging over a number of collected Doppler spectra.

The raw spectra of δ_{s} and ρ_{s} SNR are subject to noise artifacts. Correspondingly, a noise filtering is performed to remove values which are below a given threshold value

$$n = m + 3\sigma \tag{2}$$

with m being the mean and σ being the standard deviation of noise in the cross channelco-channel. The properties of the noise in the cross channel we estimate co-channel is estimated from the last 5 range gates of each profile assuming no scattering is present. All data points of δ_{s} and ρ_{s} which are lower than A spectral line with the power in the cross channel below n will be removed before any subsequent data analysis step is appliedis excluded from the following analysis.

An important technical aspect which needs to be considered in the data analysis is the leakage of a fraction of signal from the co channel into the cross channel. This depolarization channel decoupling, in terms of the integrated cross-polarization ratio (Chandrasekar and Keeler, 1993, ICPR), was found to be as low as −31 dB for the SLDR Mira-35 The co-cross-channel isolation was determined with the experimental approach described in Myagkov et al. (2015), by means of identification of the minimum SLDR value that was measured at zenith-pointing, in the presence of light drizzle. The co-cross-channel isolation used in this study , as was also confirmed in previous studies (Bühl et al., 2016; Radenz et al., 2021). The detection of $\delta_s < -31$ dB is therefore not possible and entirely caused by the depolarization channel decoupling. was thus found to be −35 dB with MIRA-35.

2.2 Dataset

MIRA-35 is operated as part of the Leipzig Aerosol and Cloud Remote Observations System (LACROS, Radenz et al. (2021)), a suite of ground-based instruments of the Leibniz Institute for Tropospheric Research (TROPOS). Besides the SLDR-mode Ka-band scanning cloud radar, LACROS comprises an extensive set of active and passive remote sensing instruments for the characterization of aerosol properties, clouds, and precipitation, including multi-wavelength polarization lidar, Doppler lidar, microwave radiometer and optical disdrometer. Data used in this study were acquired in the framework of a deployment of LACROS at the Mediterranean site of Limassol, Cyprus (34.68° N, 33.04° E, 10 m a.s.l) during the Cyprus Clouds, Aerosol and pRecipitation Experiment (CyCARE, Ansmann et al. (2019); Radenz et al. (2021)). The region of Cyprus is a relevant location for studies of the impact of aerosol on cloud processes because of a large variety of air pollutants, desert dust, and marine salt particles in the atmosphere above the island. The CyCARE campaign was conducted from September 2016 until March 2018 and aimed on the determination of the relationship between aerosol properties and the formation of cirrus and mixed-phase clouds (Ansmann et al., 2019; Radenz et al., 2021) in the heterogeneous freezing regime.

2.3 Measured SLDR and modeled δ_s and ρ_s $\widehat{\text{SLDR}}$

The VDPS method combines simulations of $\hat{\delta}_s$ $\widehat{\text{SLDR}}$ (thereby and $\hat{\rho}_s$ assuming spheroidal particle shape with measurements of the same two parameters of δ_s and ρ_s (see Section 3). Thereby and hereafter, the symbol ˆ denotes simulated parameters. In this study we use) with measurements of SLDR (see Section 3). The study is based on the same set of analytical equations for the polarimetric variables as were derived in the previous study of Myagkov et al. (2016b). Modeled $\hat{\rho}_s$ (a,b) and $\hat{\delta}_s$ (c,d) as function of polarizability ratio ξ and degree of orientation κ for particles at $\theta = 90°$ (a,c) and $\theta = 150°$ (b,d) antenna elevation angle. The red '+' designs the oblate domain, the blue 'O', the isometric domain and the green '*' the prolate particle classes, respectively, when assuming a horizontally oriented main axis. The elevation dependency of these three scenarios are depicted further in Fig. 3. equations as was previously presented by Myagkov et al. (2016a). The theoretical framework assumes Rayleigh scattering and utilizes a spheroidal approximation of particle shape (Matrosov, 1991; Ryzhkov, 2001; Bringi and Chandrasekar, 2001) . Parameters retrieved by the correlation of measured δ_s and modeled $\hat{\delta}_s$ are (Matrosov, 1991). In the used scattering model, polarimetric variables depend on two parameters: the polarizability ratio (ξ) and the degree of orientation (κ) which describe , which describes the particles by means of a density-weighted axis ratioand their preferred orientation , respectively. , and the degree of orientation κ which is a measure of the preferred orientation of the spheroids population. It is well known that the Rayleigh approximation is not always applicable to simulate scattering from large ice particles. Often the direct dipole approximation (DDA) is used to simulate scattering of individual ice particles having a complex shape. However, these simulations are often limited to a number of predefined shapes and therefore do not necessarily represent the ice particles observed by a radar. Simulations for a single particle also do not reflect the volumetric scattering effects. In general, ice particles in a scattering volume have arbitrary shapes and the contribution of individual particles to the backscattering radar observables is averaged out. We decided to assume the Rayleigh scattering and the spheroidal particle approximation (Matrosov, 1991; Ryzhkov, 2001; Bringi and Chandrasekar, 2001) because (1) such a model explains general polarimetric scattering

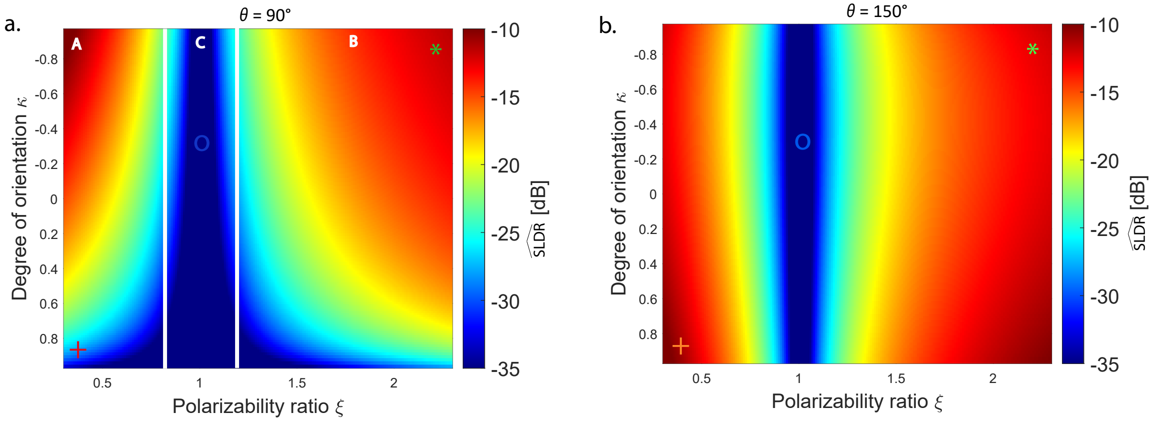

Figure 2. Modeled $\widehat{\mathrm{SLDR}}$ as function of polarizability ratio ξ and degree of orientation κ for particles at (a) $\theta = 90°$ and (b) $\theta = 150°$ antenna elevation angle. '+' (oblate particles), 'O' (isometric particles) and '*' (prolate particles) symbols are data points used in Figure 3. The elevation dependency of these three scenarios are depicted further in Section 2.3. The two white vertical lines in (a) separate the three particle domains of oblate (zone A), prolate (zone B) and the isometric (zone C) hydrometeors.

effects with just a few parameters, (2) the model parameters are well constrained by the observations, (3) the volumetric scattering is taken into account, and (4) the model allows a computationally effective derivation of the polarizability ratio.

Figure 2 shows dependencies of ~~$\hat{\delta}_\mathrm{s}$ and $\hat{\rho}_\mathrm{s}$~~ $\widehat{\mathrm{SLDR}}$ on the polarizability ratio and degree of orientation of ice particles at 90° (zenith) and 150° (60° off-zenith) elevation angle. ~~By comparing Figures 2c and 2d, it can be seen that $\hat{\delta}_\mathrm{s}$~~ 2a and 2b show that $\widehat{\mathrm{SLDR}}$ is mostly sensitive to ξ (as noted by Matrosov et al. (2001))~~. In contrast, as a comparison of Figures 2a and 2b shows, $\hat{\rho}_\mathrm{s}$ is a proxy of degree of orientation κ (as described by Ryzhkov (2001)). Indeed, $\hat{\rho}_\mathrm{s}$ features no sensitivity with respect to ξ, as gradients of $\hat{\rho}_\mathrm{s}$ against the elevation angle only exist with respect to κ.~~ , which demonstrates the relevance of using SLDR rather than ZDR to determine the particle shape. For our radar configuration, the realistic range of possible polarizability ratios ξ spans from 0.3 to 2.3 ~~giving an idea about the shape of particles, while the~~ and the degree of orientation κ ~~, ranging from -1 to 1, describes the orientation of particles.~~ is ranging from -1 to 1. κ will only be briefly elaborated in this section as it will be used only qualitatively in the frame of this study. In the case of spheroidal approximation and Rayleigh scattering regime, the polarizability ratio ξ, describing the shape of particles, is a function of permittivity and axis ratio and is independent of the particle volume. A polarizability ratio $\xi = 1$ designates spherical particles or particles with low density, while $\xi < 1$ and $\xi > 1$ describe oblate and prolate particles, respectively. Also for non-isometric particles, a decrease in apparent particle density causes ξ to approach a value of unity ~~(Myagkov et al., 2016b)~~(Myagkov et al., 2016a). The degree of orientation characterizes the width of the particle orientation angle distribution (the degree of orientation is explained in more details in Myagkov et al. (2016a), in Figure 9 and Equation 11 in there). For instance, $|\kappa| = 0$ corresponds to uniform distribution, while $|\kappa| = 1$ indicates that all particles are aligned in the same way. The sign of κ indicates the preferable orientation of the symmetry axis, i.e., $\kappa = +1$ indicates that all particles are aligned and have a vertical symmetry axis, $\kappa = -1$

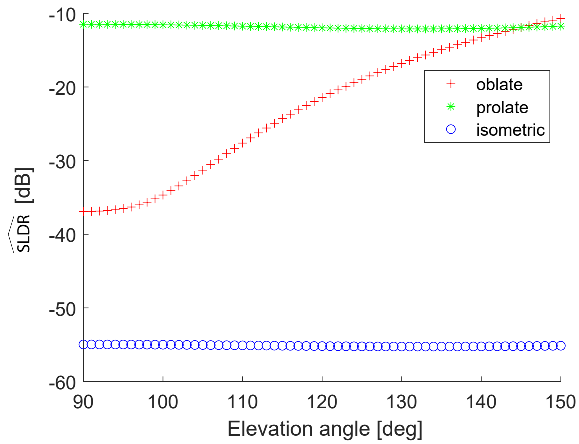

Figure 3. Modeled distributions Distributions of δ_s and ρ_s modeled $\widehat{\mathrm{SLDR}}$ as a function of elevation angle between 90° to and 150° for typical horizontally oriented oblate ("+" red), isometric ("o" blue), and prolate ("*" green) particles, respectively, issue from . The same symbols in Figure 2 illustrate the location of the data points in the model field at 90° (Figure 2a) and 150° (Figure 2b) elevation angle.

corresponds to the case when particles have a predominantly horizontally aligned symmetry axis. We therefore assume $\kappa >= 0$ for oblate particles and $\kappa <= 0$ for prolate particles. Regarding Figures 2b and 2d a and 2b we consider that $\kappa \approx -0.3$ is corresponding to radomly randomly oriented isometric particles when $\rho_s \approx 0$ and δ_s SLDR is minimal and these values do not depend on the elevation angle (Myagkov et al., 2016a).

As the goal of this paper is to derive the vertical distribution of particle shape in a cloud, which is mostly described by the polarizability ratio , this work concentrates on evaluating modeled vs. observed values of δ_s. The transition from modeled and measured δ_s and ρ_s is shown Figure 3 where the δ_s and ρ_s distribution are based on the model Figure 2. Indeed symbols A subset from Figure 2 is presented in Figure 3 in order to demonstrate the general, idealized relationship between $\widehat{\mathrm{SLDR}}$ and elevation angle for the main particle shape classes oblate ("+",), isometric ("o" and) and prolate ("-"), thereby assuming predominantly horizontal orientation. Indeed, the "+" symbol is located in the oblate domain (zone A) described by a polarizability ratio $\xi = 0.35$ and a degree of orientation $\kappa = 0.85$ representing horizontally oriented plate-like particles, while the "*" represent oblate, isometric and prolate particles , respectively. This method is based on symbol is located in the prolate domain (zone B) described by $\xi = 2.15$ and $\kappa = -0.85$ representing horizontally oriented columnar crystals. The Symbol "o" is determined by $\xi = 1$ and $\kappa = -0.4$, such as randomly oriented spherical particles like liquid droplets (Myagkov et al., 2016a) , which is representative for the isometric domain (zone C). A value of $\widehat{\mathrm{SLDR}}$ is derived for all elevation angles from 90° and 150°, leading to Figure 3 which links our study to findings of Matrosov et al. (2012) , who showed showing distinct elevation-dependent signatures of δ_s SLDR for particles with different shapes. As illustrated in Figure 3, oblate particles are characterized by a positive gradient of both δ_s and ρ_s from 90° to 150° elevation angle, while prolate particles are characterized by nearly constant and relatively high values of δ_s (around -20 dB for standard columns and -15 SLDR at all elevation angles, which reach values of around −25 dB for solid columns and more than −20 dB for pronounced needles of high axis ratio) and a positive gradient of ρ_s. Nearly spherical particles are described by a low gradient of both polarimetric parameters δ_s and ρ_s (Figure 3). Dendritic particlesproduce scattering similar to isometric particles when pointing to the zenith ((Reinking et al., 2002; Matrosov et al., 2012). The isometric primary particle shape class is represented by constantly low values of SLDR at all elevation angles between 90° elevation angle). But the dendritesto 150°. Finally, plate-like particles, belonging to the oblate particle class, known to align predominantly horizontally along their planar planes, produce scattering similar to isometric particles observed at zenith-pointing (90° elevation angle) and will increasingly appear oblate at a low elevation anglelow elevation angles. That is why in the case of dendrites, $\delta_s$plate-like hydrometeors, SLDR, representative of the particle shape, is minimal at zenith pointing zenith-pointing and increases until 150° elevation angle. ρ_s for horizontally aligned dendrites is expected to increase while scanning from 90° to 150° elevation angle. Indeedat zenith pointing dendrites , at zenith-pointing, plate-like crystals have random orientation in the polarization plane, while at a low elevation angle horizontally aligned particles produce rather coherent returns in both polarimetric channels. Finally, the isometric primary particle shape class containing droplets, aggregates and graupel is represented by constantly low values of δ_s and ρ_s at all angles between 90° and 150° elevation angle. Note, that it is not directly possible to classify the type of isometric particles (i.e. aggregate or rimed particlee.g., aggregates or rimed particles can be isometric particles, too) since they have similar angular polarimetric signatures at all elevation angles. Discrimination between these types of particles can be donee.g. , e.g., using multiple-frequency observations (Kneifel et al. (2016)) (Kneifel et al., 2016) but this is out of the scope of the current study. VDPS method aims to differentiate these three the three main particle shape classes and their vertical evolution within cloud systems in order to determine microphysical processes occurring in mixed-phase clouds.

3 Methodology

The concept of the VDPS approach is to realize a tailored retrieval of the vertical distribution of particle shape. The VDPS method, adapted for the SLDR-mode scanning cloud radar as introduced in Section 2.1, has the particularity of combining simulated and measured values of δ_s at only the SLDR at only two elevation anglesof 90° and 150° . Availability of a shape retrieval for only two elevation angles would allow much shorter scan cycles compared to the full RHI scans utilized in earlier studies such as of Myagkov et al. (2016b). , isolated from a full RHI scan. As the VDPS method relies on polarimetric measurements at different elevation angles, horizontal homogeneity of the observed clouds is required. In this study, this prerequisite is achieved by means of a combination of experienced-eye evaluation of the obtained RHI scans and the requirement of a The scale of the horizontal homogeneity is defined by the maximum observation distance of the used cloud radar and the lowest elevation angle (10–15 km and 30°, respectively). Thus, the required scale of the horizontal homogeneity is mostly below 13 km, which is comparable, e.g., to a footprint of spaceborne remote-sensing meteorological instruments. A majority of stratiform clouds have much larger spatial scale. In addition, the algorithm requires a minimum number of data points in each layer, representing 15% of the total amount of data points, as will be explained in Section ??. 3.1.

The general flow chart describing the three-step procedure is depicted in Figure 4. Within the first step, presented in Section ~~??, the data~~ 3.1, the dataset is prepared for ~~evaluation against a spheroid scattering model , presented~~ the evaluation against the spheroidal scattering model in Section 3.2. By combination of ~~this model with~~ $\widehat{\mathrm{SLDR}}$ simulated by the spheroidal scattering model with SLDR observations, the range of possible primary particle shape classes is identified and the associated uncertainties are assessed in Section 3.2. In the final step presented in Section 3.3, ~~gradients calculated in Section ?? are~~ linear regressions of SLDR vs. elevation angle are calculated and deployed to identify ~~only one possibility of the three general~~ the correct primary particle shape ~~classes, in order~~ class and to assign the proper polarizability ratio ξ ~~and quantify the primary particle shape class~~ from the set of possible solutions determined in Section 3.2.

3.1 ~~Construction~~ Determination of ~~polarimetric gradients~~ SLDR at the boundaries of the elevation range

For each of the four individual scan patterns described in Figure ~~2~~1, the returned signals in the co- and cross-channel ~~$\dot{S}_{\mathrm{co}}(\omega_k)$ and $\dot{S}_{\mathrm{cx}}(\omega_k)$~~ $P_{\mathrm{co}}(\omega_k)$ and $P_{\mathrm{cx}}(\omega_k)$, respectively, collected by MIRA-35 are saved in a level-0 file, in the pdm format defined by Metek company. Consequently, the pdm data are in a first step converted into NetCDF format containing the polarimetric measurements of ~~$\delta_{\mathrm{s}}(\omega_k)$ and $\rho_{\mathrm{s}}(\omega_k)$~~ $\mathrm{SLDR}(\omega_{\mathrm{k}})$, calculated with ~~equations~~ Equation (1)~~and (??), respectively,~~ , as well as ~~θ~~ elevation angle and range. Next, the noise filtering (equation (2)) is applied as explained in Section 2.3 and only the maximum spectral component of the remaining noise-free spectra are selected. Thus, arrays ~~of δ_{s} and ρ_{s} are obtained which depend on~~ containing one value of SLDR per elevation angle are obtained for each granule of time and range. All range values are converted into height above ground, using the elevation angle θ as additional input. The VDPS algorithm runs automatically for each selected RHI scan. A main loop is used to separate the observations into multiple vertical 'height' layers. In general, any ~~arbitary~~ arbitrary value of height resolution can be chosen. For the current study, each height step corresponds to the range resolution of MIRA-35 (31,18 m, i.e., the height resolution at zenith-pointing), similar to as was done by ~~Myagkov et al. (2016b)~~ Myagkov et al. (2016a). The following procedure is performed for each height layer which contains at least 20 ~~Doppler spectra of δ_{s}~~values of SLDR from a full RHI scan recorded from 90° to 150° elevation angle (Figure 1). The value of 20 points per layer represents about 15% of the maximal number of data points~~in one vector~~. If this limit is not reached, it could mean that no cloud was detected at this layer or that not enough particles are contained at the investigated height level of the cloud~~layer, which will~~ , which would influence the quality of results. In this situation, the procedure will be stopped only for this layer at this step (no results are produced) and will continue to iterate into the next layer. If a sufficient amount of data points was found at a height level, ~~new vectors of $\delta_{\mathrm{s}}(H,\theta)$ and $\rho_{\mathrm{s}}(H,\theta)$ are built.~~ a new vector of $\mathrm{SLDR}(\mathrm{H},\theta)$ is built. The elevation range of $\mathrm{SLDR}(\mathrm{H},\theta)$ does thus not necessarily span the full elevation range of the RHI scan, as some data points at the elevation limits might have been removed.

As shown in ~~Fig.~~ Figure 3 and as will be elaborated further in Section 3.3, polarimetric signatures of different particle shapes are most visible when the elevation angle difference of the performed scans is large. For this reason, ~~it is sufficient to use values of the polarimetric parameters δ_{s} and ρ_{s} only at 90° and 150° elevation angle. The VDPS algorithm runs automatically for each selected RHI scan.~~ a full RHI scan is used to verify the homogeneity of the investigated cloud (Section 3.1) and to calculate the SLDR linear regression (Section 3.3), but only values of SLDR at two elevation angles are needed in the model output (Section

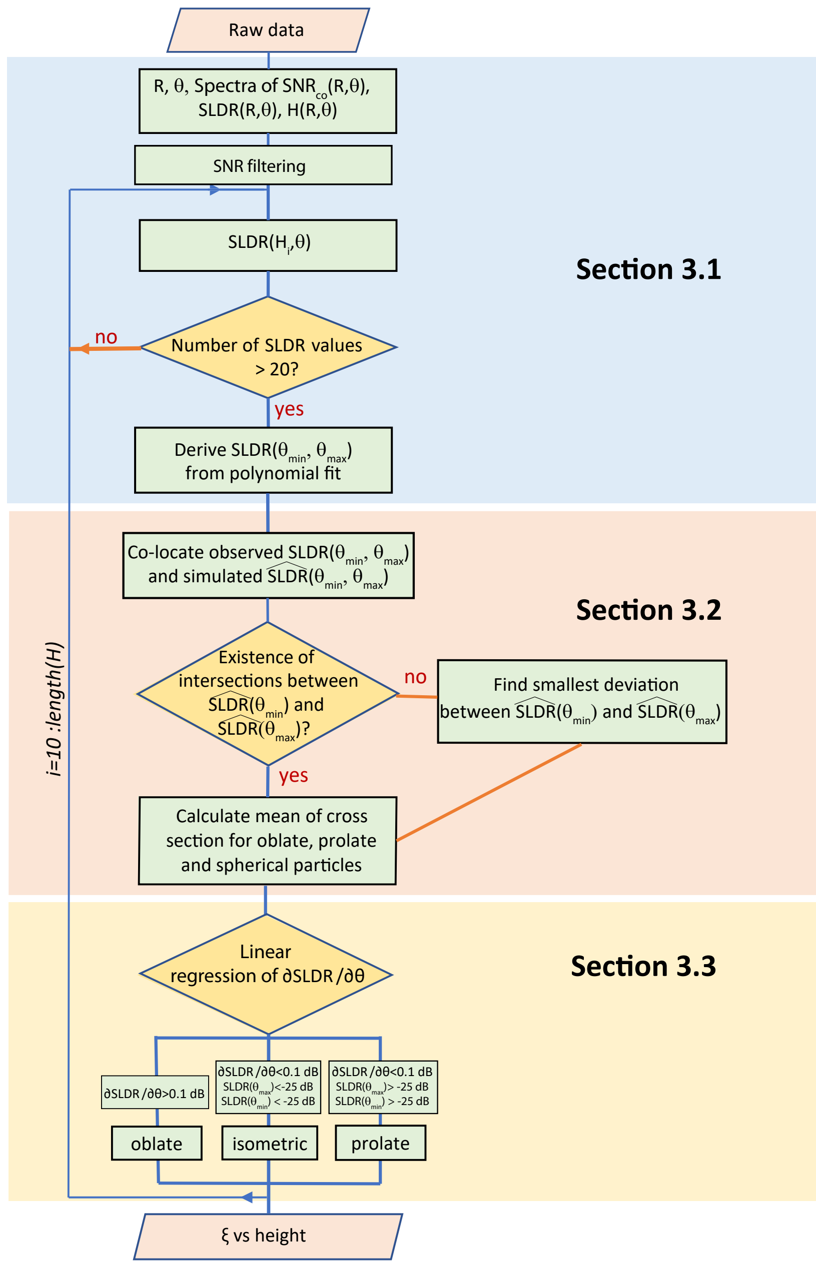

Figure 4. Flowchart describing the VDPS method.

3.2). In order to be as efficient as possibleprepare the observational input for the evaluation against the spheroidal scattering model to be described in Section 3.2, we will look for the data points of δ_{s} associated with the smallest values of elevation angles SLDR associated to the smallest observed value of elevation angle ($\theta_{\min}$, usually zenith-pointing) and those with the largest values of elevation angles to the largest value of elevation angle ($\theta_{\max}$, usually 150°). Thus, in a next step, fit values of measured δ_{s} SLDR at the minimum elevation angle $\theta_{\min}$, ($\delta_{\mathrm{s}}(\theta_{\min})$) , (SLDR($\theta_{\min}$)) and at maximum elevation angle $\theta_{\max}$, ($\delta_{\mathrm{s}}(\theta_{\max})$) , (SLDR($\theta_{\max}$)) are calculated. These notations will be used further in Section 3.2. It can be seen in Figure 3, that the modeled slope of the derived curve is never straight for δ_{s}, relationship between SLDR and elevation angle is not linear for SLDR, especially in the case of oblate particles, and the more appropriate fit to calculate $\delta_{\mathrm{s}}(\theta_{\min})$ and $\delta_{\mathrm{s}}(\theta_{\max})$ for this case method to calculate SLDR($\theta_{\min}$) and SLDR($\theta_{\max}$) for all cases is to use a 3rd degree polynomial fit. As reminder, we focus only on the particle shape in this paper, that is why we will only use the fit values of $\delta_{\mathrm{s}}(\theta_{\min})$ SLDR($\theta_{\min}$) and $\delta_{\mathrm{s}}(\theta_{\max})$ which depends primarily on the particle shape, while ρ_{s} describes the orientation of particles (Section 3.2) . $\delta_{\mathrm{s}}(\theta_{\min})$ and $\delta_{\mathrm{s}}(\theta_{\max})$ SLDR($\theta_{\max}$) are determined with the fit values from the 3rd degrees polynomial fit at $\theta_{\min}$ and $\theta_{\max}$, respectively. As an example, Figure 5 shows the distribution of SLDR from $\theta_{\min}$ to $\theta_{\max}$. Values of SLDR($\theta_{\min}$) and SLDR($\theta_{\max}$) are readable at 90° ($\theta_{\min}$) and 150° ($\theta_{\max}$) elevation angle as SLDR($\theta_{\min}$) = −32 dB and SLDR($\theta_{\max}$) = −11 dB. SLDR($\theta_{\min}$) and SLDR($\theta_{\max}$) are saved and will be utilized in Section 3.2 for the evaluation against the spheroidal scattering model as presented in Section 3.2, for compiled at the same elevation angles $\theta_{\min}$ and $\theta_{\max}$. In parallel we will calculate mean gradients $\frac{\partial \delta_{\mathrm{s}}}{\partial \theta}$ and $\frac{\partial \rho_{\mathrm{s}}}{\partial \theta}$ estimated with a linear regression. The derived linear gradients are used to define the primary particle shape class, as will be described in Section 3.3.

3.2 Combination Estimation of modeled and measured polarimetric parametersthe polarizability ratio for each layer

The second section In the first step of the VDPS retrieval is dedicated to the comparison of measured (Section ??) and modeled polarimetric parameters (Section 2.3). The original we find two SLDR values corresponding to $\theta_{\min}$ and $\theta_{\max}$ (Section 3.1). In the second step we search for values of the polarizability ratio and the degree of orientation for which the simulated $\widehat{\mathrm{SLDR}}$ fits to SLDR($\theta_{\min}$) and SLDR($\theta_{\max}$).

The original spheroidal scattering model based on Myagkov et al. (2016b) Myagkov et al. (2016a) does not take into account hardware-related effects and, therefore, predicts minimum values of $\hat{\delta}_{\mathrm{s}}$ $\widehat{\mathrm{SLDR}}$ that cannot be reached with the current radar technology . As explained Section 2.1, the detection of $\delta s < -31$ dB is not possible. This adaptation is visible in Figures 2c and 2d with the extended blue domain in the middle, representing for this case, the minimum modeled $\hat{\delta}_{\mathrm{s}}$ values around −30 dB. The lower sensitivity of our radar compared to the modeled values implies an increase of imprecision concerning isometric particles or particles of low density ($\xi = 1$)due to the polarimetric coupling in the antenna system. The polarimetric coupling (co-cross channel isolation) of the used radar is −35 dB, as mentioned in Section 2.1, and leads to an increased uncertainty of the retrieval for particles with polarizability ratio between 0.9 and 1.1. The modeled distribution of $\hat{\delta}_{\mathrm{s}}$ and $\hat{\rho}_{\mathrm{s}}$ $\widehat{\mathrm{SLDR}}$ from 90° to 150° elevation angle for three exemplary particle habits from oblate, isometric, and prolate particle shape classes, are illustrated in the earlier introduced Figure 3. This graphic represents the theoretical aspect of the expected gradient in these relationship between $\widehat{\mathrm{SLDR}}$ and elevation angle in the three different primary particle shape classes, which can be reproduced with is about to be faced with the direct measurements of δ_s and ρ_s. The SLDR. In the second part of this subsection is dedicated to section, we compare the modeled $\hat{\delta}_s$ with $\delta_s(\theta_{min})$ and $\delta_s(\theta_{max})$ from direct measurements, processed in Section ??, at θ_{min} and θ_{max} (Figure 6). $\delta_s(\theta_{min})$ and $\delta_s(\theta_{max})$ are calculated from the 3rd order $\widehat{SLDR}$ and measured SLDR obtained from the polynomial fit (ref Section??) at Section 3.1) at elevation angles θ_{min} and θ_{max}, respectively.

as explained in Section 3.1. In order to consider potential measurement inaccuracies, the 95% prediction interval confidence interval Δ_{95} of the polynomial fit will be used to determine the potential range of the intersection. The confidence interval is calculated as follows:

$$\Delta_{95} = 2\Delta \qquad (3)$$

where Δ is the standard deviation of the difference between the measured and simulated values of SLDR at all available elevation angles from 90° to 150°. The model is processed for at θ_{min} and θ_{max} and the algorithm identifies isolines of $\delta_s(\theta_{min})$ $SLDR(\theta_{min}) = \widehat{SLDR}(\theta_{min})$ $\pm$ the 95% interval prediction, and $\delta_s(\theta_{max})$ Δ_{95}, and $SLDR(\theta_{max}) = \widehat{SLDR}(\theta_{max})$ $\pm$ the 95% interval predictionΔ_{95}, in the modeled fields of $\hat{\delta}_s$ $\widehat{SLDR}$ at θ_{min} and θ_{max}, respectively, such as shown . For example, in Figure 6a and 6b . Intersections between $\hat{\delta}_s(\theta_{min})$ and $\hat{\delta}_s(\theta_{max})$ will appear in the model output (we can see the isoline where $SLDR(\theta_{min}) = \widehat{SLDR}(\theta_{min})$ plotted in red and the isoline where $SLDR(\theta_{max}) = \widehat{SLDR}(\theta_{max})$ plotted in blue on the model, respectively. The two isolines are plotted together in Figure 6c) and the associated values of ξ and κ are identified. , highlighting intersections between $\widehat{SLDR}(\theta_{min})$, shown as red curve, and $\widehat{SLDR}(\theta_{max})$, shown as blue curve, resulting in $\xi = 0.45$ and $\xi = 2$. If no intersection is found between $\hat{\delta}_s(\theta_{min})$ and $\hat{\delta}_s(\theta_{max})$$\widehat{SLDR}(\theta_{min})$ and $\widehat{SLDR}(\theta_{max})$, the algorithm searches for the point where the difference between $\hat{\delta}_s(\theta_{min})$ and $\hat{\delta}_s(\theta_{max})$ $\widehat{SLDR}(\theta_{min})$ and $\widehat{SLDR}(\theta_{max})$ is the lowest. Finally, the algorithm characterizes the x-axis positions (polarizability ratio ξ) by deriving the mean and standard deviation of all overlapping data points included in each intersection between the isolines of $\widehat{SLDR}(\theta_{min})$ and $\widehat{SLDR}(\theta_{max})$ (Figure 6). The Three values of ξ for each intersection are saved at each height iteration . In the final step, as described in Section 3.3, the appropriate corresponding to the three primary particle shape classes : the first intersection in the oblate particle shape class with $\xi < 1$ ($\xi = 0.45$ in Figure 6c), the second intersection for the prolate particle shape class will be identified and the remaining, corresponding value of polarizability ratio will be attributed as solution. with $\xi > 1$ ($\xi = 2$ in Figure 6c) and a mean of these two intersections for the isometric or low-density particle shape class with $\xi \approx 1$. The procedure could be repeated in a similar manner for determination of the possible y-axis values, which are the possible solutions of the degree of orientation κ, which is however not in the scope of our study.

3.3 Identification and quantification of the primary particle shape classesclass

The processing steps conducted in Section 3.2 result in the provision of two intersections of $\hat{\delta}_s(\theta_{min})$ and $\hat{\delta}_s(\theta_{max})$, as is illustrated in Figure 6. Consequently, a possible solution for ξ exists for each primary particle shape class. The The last step of the VDPS method is thus to identify the consists of the identification of the primary particle shape class among the three possible solutions introduced in Section 3.2 and to quantify the primary particle shape class with the assigned value of ξ.

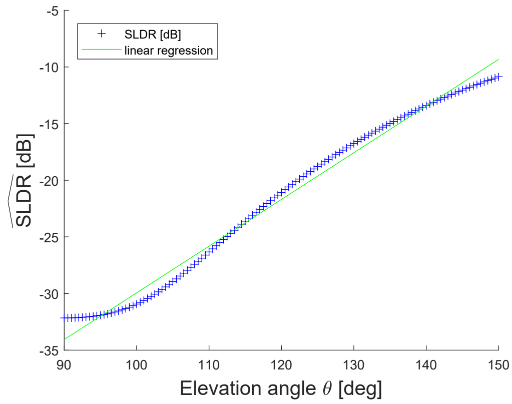

Figure 5. ~~Determination~~ Distribution of ~~the possible values of ξ by searching for the intersections of observed δ_s in the data fields simulated with the spheroidal scattering model at (~~$\widehat{\text{SLDR}}$ as a ~~) $\theta_{\text{min}} = 90^\circ$ and (b) $\theta_{\text{max}} = 150^\circ$~~ function of elevation angle ~~. The red~~ between $\theta_{\text{min}} = 90^\circ$ and ~~blue curves in (a) and (b) depict~~ $\theta_{\text{max}} = 150^\circ$ for the ~~isolines of the observed values~~ same dendritic crystal population as presented in ~~the model space at 90° and 150° elevation~~Figure 6 : $\text{SLDR}(\theta_{\text{min}}) = -32\text{dB}$, ~~respectively. In (c) the overlay of the intersections of the isolines for 90° and 150° is shown. As observational input~~$\text{SLDR}(\theta_{\text{max}}) = -11\text{dB}$, ~~hypothetical values of typical oblate particles with $\delta_s(\theta_{\text{min}}) = -32dB$~~ and ~~$\delta_s(\theta_{\text{max}}) = -11dB$ were selected~~$\kappa = 0.85$. The green line represents the SLDR linear regression calculated in Section 3.3.

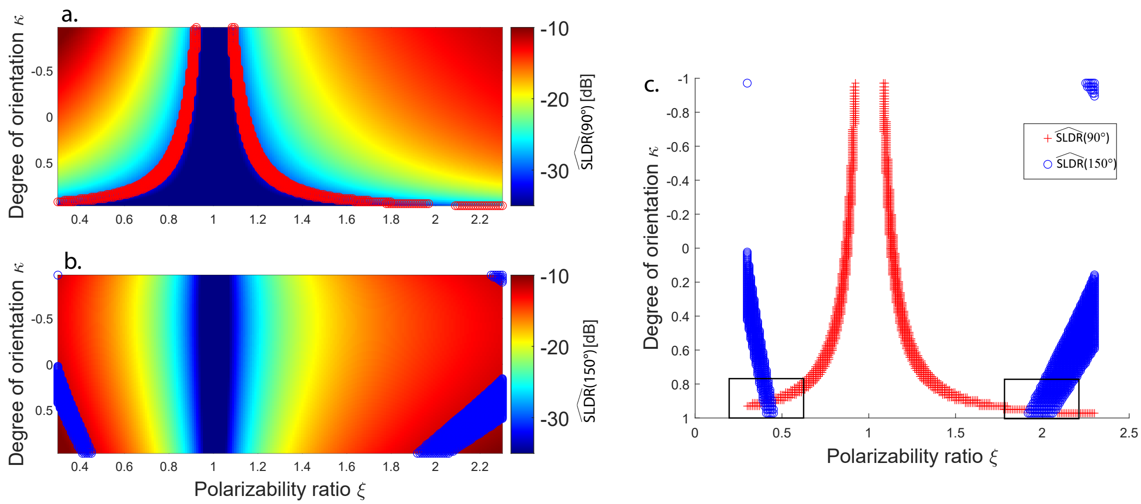

Figure 6. Determination of the possible values of ξ by searching for the intersections between $\widehat{\text{SLDR}}(\theta_{\text{min}})$ and $\widehat{\text{SLDR}}(\theta_{\text{max}})$ on the spheroidal scattering model at (a) $\theta_{\text{min}} = 90^\circ$ and (b) $\theta_{\text{max}} = 150^\circ$ elevation angle. The red and blue curves in (a), (b) and (c) depict the isolines as (a) $\text{SLDR}(\theta_{\text{min}}) = \widehat{\text{SLDR}}(\theta_{\text{min}})$ and (b) $\text{SLDR}(\theta_{\text{max}}) = \widehat{\text{SLDR}}(\theta_{\text{max}})$ at 90° and 150° elevation, respectively. In (c) the intersections of the $\widehat{\text{SLDR}}(\theta_{\text{min}})$ and $\widehat{\text{SLDR}}(\theta_{\text{max}})$ isolines are shown. As input, hypothetical values of typical oblate particles with $\text{SLDR}(\theta_{\text{min}}) = -32\text{dB}$ and $\text{SLDR}(\theta_{\text{max}}) = -11\text{dB}$ were selected.

As introduced in Section 2.3, the relationship between δ_s, ρ_s SLDR and the elevation angle is an important aspect to determine the polarizability ratio ξ (Matrosov et al., 2012) particle shape (Reinking et al., 2002; Matrosov et al., 2005, 2012) and will be used in the following to discriminate between the primary shape classes. Based on the comparison between the modeled and observed data from case studies representing the three particle shape classes, thresholds of $\frac{\partial \delta_s}{\partial \theta}$ and $\frac{\partial \rho_s}{\partial \theta}$ were . A threshold of $\frac{\partial \mathrm{SLDR}}{\partial \theta}$ is determined in such a way that they allow for an unambiguous separation of the prolate, oblate and isometric hydrometeor shape classes is possible, by applying a robust linear fit to all observed pairs of SLDR and elevation angle. The resulting limit values were derived to be $lim_{\delta s} = 0.1$ and $lim_{\rho s} = 0.005$. $lim_{\mathrm{SLDR}} = 0.1$ dB, as a threshold describing a certain change of the SLDR in dB per degree of elevation angle, and $lim_{\mathrm{pro}} = -25$ dB, which describes the maximum value of SLDR to be associated to the prolate shape class. It should be noted that the two limit values might depend on the individual radar calibration. The actual shape class selection criteria are summarized in Table 2 and are described in the following. If the slopes of $\frac{\partial \delta_s}{\partial \theta}$ and $\frac{\partial \rho_s}{\partial \theta}$ exceed $lim_{\delta s}$ and $lim_{\rho s}$, respectively, linear regression $\frac{\partial \mathrm{SLDR}}{\partial \theta}$ exceeds lim_{SLDR}, particles are assigned to the oblate primary particle shape class. If the slope of only $\frac{\partial \rho_s}{\partial \theta}$ exceeds $lim_{\rho s}$ and δ_s is relatively high, generally over -25 dB, but constant with a slope below $lim_{\rho s}$, $\frac{\partial \mathrm{SLDR}}{\partial \theta}$ doesn't exceed lim_{SLDR} as well as $\mathrm{SLDR}(\theta_{\mathrm{min}})$ and $\mathrm{SLDR}(\theta_{\mathrm{max}})$ exceed lim_{pro}, particles are assigned to the prolate primary particle shape class. If both gradients are below lim_{δ_s} $\frac{\partial \mathrm{SLDR}}{\partial \theta}$ doesn't exceed lim_{SLDR} as well as $\mathrm{SLDR}(\theta_{\mathrm{min}})$ and $lim_{\rho s}$ for both polarimetric parameters $\mathrm{SLDR}(\theta_{\mathrm{max}})$ are below lim_{pro}, particles are associated to the isometric primary particle shape class. If particles are assigned to the isometric particle shape class, ξ will be calculated with a as the mean of the associated values of ξ contained in both intersections of $\hat{\delta}_s(\theta_{\mathrm{min}})$ and $\hat{\delta}_s(\theta_{\mathrm{max}})$ $\widehat{\mathrm{SLDR}}(\theta_{\mathrm{min}})$ and $\widehat{\mathrm{SLDR}}(\theta_{\mathrm{max}})$ on both sides of $\xi = 1$ (Section 3.2). In the oblate and prolate primary particle shape classes, the error bars are calculated based on the intersections of the standard deviation obtained for $\hat{\delta}_s(\theta_{\mathrm{min}})$ and $\hat{\delta}_s(\theta_{\mathrm{max}})$ $\widehat{\mathrm{SLDR}}(\theta_{\mathrm{min}})$ and $\widehat{\mathrm{SLDR}}(\theta_{\mathrm{max}})$, following the same procedure as explained in Sections 3.2and 3.3Section 3.2. Concerning the isometric primary particle shape class, ξ values of the two intersections identified before are used as error bars.

By putting the gradients of $\frac{\partial \delta_s}{\partial \theta}$ and $\frac{\partial \rho_s}{\partial \theta}$ into context to the shape-dependent limit numbers ($lim_{\delta s}$ and $lim_{\rho s}$), only one value of ξ is assigned to the previously identified primary particle shape class. Subsequently, the variability of the particle shapes in the selected primary particle shape class can be derived and applied to further data analysis steps. Figure 6 describes the comparison of the measured δ_s with $\hat{\delta}_s$ from the spheroidal scattering model using the VDPS method developed in Section 3.2. As an example a hypothetical case study where $\delta_s(\theta_{\mathrm{min}}) = -32$ dB and $\delta_s(\theta_{\mathrm{max}}) = -11$ dB was chosen, representing oblate particles like dendrites as Figure 5 depicts the relationship between SLDR and elevation angle from θ_{min} to θ_{max}. According to Reinking et al. (2002) and Matrosov et al. (2012), the found relationship is representative for oblate particles such as as plate-like crystals, as depicted in Table 2. Regarding Figure 6bc presented in Section 3.2, we observe two intersections on both sides of ξ=1 $\xi = 1$ and the choice of one of them requires an evaluation of the gradients of δ_s and ρ_s linear regression of SLDR from θ_{min} to θ_{max}. The associated gradients of the hypothetical values of δ_s and ρ_s distribution of SLDR presented in Figure 5 confirm confirms the assignment of ice particles in the primary oblate to the oblate primary particle shape class due to the increase of both δ_s and ρ_s exceeding $lim_{\delta s}$ and $lim_{\rho s}$ SLDR from θ_{min} to θ_{max} . and the exceeding of lim_{SLDR}. A value of $\xi = 0.45$ is finally derived for this layer. The last step, according to the flow chart depicted in Figure 4, is to store the distribution of ξ previously calculated in Section 3.2over the entire height of the cloud's profileapply the classification to the previously calculated profile of ξ (see Section 3.2) and to store the selected values. This distribution of particle shape delivers information about the stratification vertical profile of ice particle shapes in a cloud which is a relevant indicator to understand in-cloud processes, illustrated in Section 4.4. The next section aims to evaluate and validate this new developed approach, the VDPS method , by means of three case studies, representing the three previously described particle shape classes prolate, oblate, and isometric, and demonstrate the ability of the VDPS method to detect microphysical processes.

Gradient of (a) δ_s and (b) ρ_s as a function of elevation angle between $\theta_{min} = 90°$ and $\theta_{max} = 150°$ for the same hypothetic dendritic crystal population as presented in Fig. 6.

4 Results

In this Section, we will demonstrate the capabilities of the VDPS retrieval by means of three case studies associated with the three main particle shape classes isometric (rain, Section 4.1), prolate (columnar ice crystals, Section 4.2) and oblate (dendritic plate-like ice crystals, Section 4.3). The three A fourth case study is presented in Section 4.4 to conclude and open the discussion concerning the ability of VDPS to describe microphysical processes by a change in particle shape from cloud top to cloud base. The four case studies were selected from the CyCARE observations, presented in Section 2. Temperature provides an important constraint for the particle shape, since laboratory studies show a clear relationship between particle shape, temperature and supersaturation with respect to ice (Bailey and Hallett, 2009)(Bailey and Hallett, 2009; Myagkov et al., 2016b). Given conditions of liquid water saturation, near $T = -2°C$, the growth is plate-like, near $T = -5°C$ the growth is columnar, near $T = -15°C$ the growth again becomes plate-like and at lower temperature, the growth becomes a mixture of thick plates and columns. A general meteorological situation is presented for each case study using the Cloudnet classification of targets based on MIRA-35 at zenith pointing zenith-pointing and auxilliary instrumentation (Illingworth et al., 2007) and two RHI-scans of δ_s and ρ_s a RHI scan of SLDR from θ_{min} to θ_{max}. Subsequently, the two polarimetric parameters δ_s and ρ_s polarimetric parameter SLDR measured at θ_{min} and θ_{max} are is combined with the spheroid spheroidal scattering model introduced in Section 3.2. We will

Table 2. Assignment of the characteristic values of δ_s and ρ_s SLDR at $\theta_{min} = 90°$ and $\theta_{max} = 150°$ elevation angle and their gradients linear regressions as function of θ. The associated typical ranges of ξ are given, as well. Please note, values of $\delta_s(\theta_{min})$ SLDR(θ_{min}) and $\delta_s(\theta_{max})$ SLDR(θ_{max}) for the isometric shape class correspond to the detection limit of SLDR SLDR (See Section 22.1). The limit values are $lim_{\delta s} = 0.1$ $lim_{SLDR} = 0.1$ dB and $lim_{\rho s} = 0.005$ $lim_{pro} = -25$ dB.

Shape class	Gradient Linear regression	Value at 90°	Val
Oblate	$\frac{\partial \delta_s}{\partial \theta}$ $\frac{\partial SLDR}{\partial \theta} > lim_{\delta s}$ lim_{SLDR}	$\delta_s(\theta_{min})$ SLDR(θ_{min}) = -30 dB	$\delta_s(\theta_{max})$ SL
$\frac{\partial \rho_s}{\partial \theta} > lim_{\rho s}$ $\rho_s(\theta_{min}) = 0$ $\rho_s(\theta_{max}) = 1$ heightIsometric	$\frac{\partial \delta_s}{\partial \theta}$ $\frac{\partial SLDR}{\partial \theta} < lim_{\delta s}$ lim_{SLDR}	$\delta_s(\theta_{max})$ SLDR(θ_{max}) = -31 -35 dB	$\delta_s(\theta_{min})$ SLD
$\frac{\partial \rho_s}{\partial \theta} < lim_{\rho s}$ $\rho_s(\theta_{min}) = 0$ $\rho_s(\theta_{max}) = 0.1$ heightProlate	$\frac{\partial \delta_s}{\partial \theta}$ $\frac{\partial SLDR}{\partial \theta} < lim_{\delta s}$ lim_{SLDR}	$\delta_s(\theta_{min})$ SLDR(θ_{min}) = -20 dB	$\delta_s(\theta_{max})$ SLD
$\frac{\partial \rho_s}{\partial \theta} > lim_{\rho s}$ $\rho_s(\theta_{min}) = 0$ $\rho_s(\theta_{max}) = 0.7$			

focus ~~on the only one~~ only on the selected layer to illustrate the case studies even though all layers are processed to obtain the vertical distribution of particle shape. The last step aims to deliver insights ~~in~~ into the quantification of the primary particle shape classes, as explained in Section 3.3, with the vertical distribution of ξ in the investigated cloud. Since the proposed method uses the spheroidal approximation of pure-ice particles and assumes Rayleigh scattering, the derived values of ξ should be analyzed with care when the method is applied to rain and the melting layer. Since rain droplets corresponding to the maximum spectral line are often near spherical, ξ is valid since for spherical particles it is not ~~strongly affected by~~ sensitive to the refractive index. In contrast, ξ in the melting layer is likely not valid, because the depolarization observed in the melting layer is not caused by columnar shapes of particles but by particle's strongly irregular shapes, water coating ~~, and~~ (and associated fluctuations of apparent density), and their large size.

~~This Section~~ This section aims to demonstrate that the VDPS method gives concordant results with the observations for the three primary particle shape classes, isometric, prolate and oblate particles, introduced in Section 3.2, and that it is a promising supplemental technique for studying cloud microphysical processes.

4.1 Isometric particle shape class: Rain event on 13 February 2017 at 13:31 UTC

The first case study concentrates on the occurrence of rain, i.e., hydrometeors representative for the primary isometric particle shape class. Measurements were recorded on 13 February 2017 ~~at~~ during an RHI scan from 13:31 to 13:33 UTC at Limassol. The studied cloud ~~presented in the blue box of~~ system, enframed by the the black box in the Cloudnet target classification mask shown in Figure 7, was identified to contain rain droplets at heights between 300 m ~~to 1200~~and 1300 m. ~~Above, a melting layer was present while further above ice particles where identified up to 4000~~The sudden drop of the melting layer height from 1300 m to around 1000 m height that is visible right at the time of the RHI scan, is an artifact of the melting layer detection scheme of Cloudnet, which switched from a fall-velocity-based detection to the 0°C-dewpoint level as threshold for the melting layer identification. However, the actual melting layer is well recognizable in Figure 8 by means of the observed high values of SLDR at around 1300 m height. The Cloudnet classification indicates a ~~mixed phase~~ mixed-phase layer at 1800 m height. ~~We~~ For this case study, we are particularly interested in the rain from 300 m to 1200 m height.

~~Figure 8a shows two RHI-scans of δ_s and ρ_s~~

Figure 8 shows the RHI scan of SLDR from 90° to 150° elevation angle which were performed at 13:31 UTC. Values of ~~δ_s~~ SLDR from $\theta_{\min}$ to $\theta_{\max}$ are low (around -30 dB) and constant at heights below the melting layer~~. In Figures 8a and 8b, both δ_s and ρ_s are relatively constant from $\theta_{\min}$ to $\theta_{\max}$~~, which is in agreement to what can be expected from scattering by isometric particles, as explained in Section 3.3. To illustrate this case study, we will focus only on one layer located at the height level from 868 m to 899 m, represented by the black line on the y-axis in Figure 8. In Figure 9b, the intersection of ~~$\hat{\delta}_s(\theta_{\min})$ and $\hat{\delta}_s(\theta_{\max})$~~ $\widehat{\mathrm{SLDR}}(\theta_{\min})$ and $\widehat{\mathrm{SLDR}}(\theta_{\max})$ is detectable by the red and blue curves which match the data of ~~δ_s~~ SLDR at $\theta_{\min}$ and $\theta_{\max}$, respectively, with the simulated data $\widehat{\mathrm{SLDR}}$ from the spheroidal scattering model. We can distinctly notice the presence of two intersections between ~~$\hat{\delta}_s(\theta_{\min})$ and $\hat{\delta}_s(\theta_{\max})$~~ $\widehat{\mathrm{SLDR}}(\theta_{\min})$ and $\widehat{\mathrm{SLDR}}(\theta_{\max})$ from either side of the dashed red line, ~~for~~ resulting in $\xi = 0.9$ and $\xi = 1.1$. In Figure 9a, the ~~gradient $\frac{\partial \delta_s}{\partial \theta}$ is constant from~~ slope of the linear regression $\frac{\partial \mathrm{SLDR}}{\partial \theta}$ is constant between $\theta_{\min}$ ~~to~~ and $\theta_{\max}$ where ~~$\frac{\partial \delta_s}{\partial \theta} < lim_{\delta s}$ and , in Figure 9b, the gradient of ρ_s is weakly~~

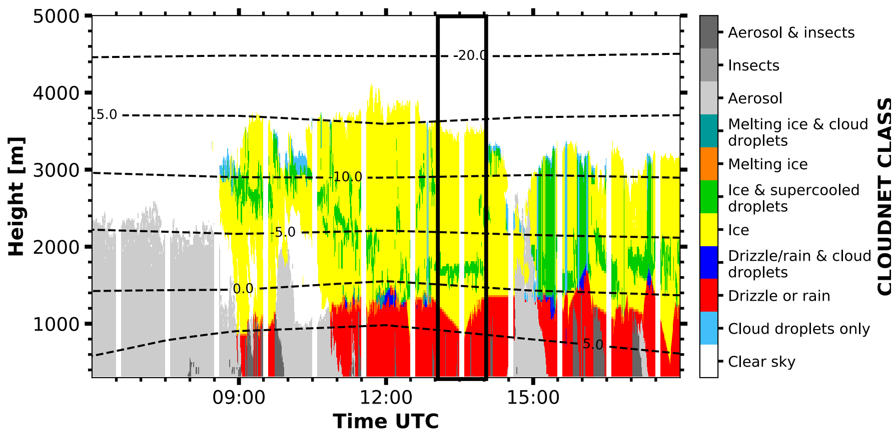

Figure 7. Cloudnet target classification mask as derived from observations at Limassol on 13 February 2017 from ~~08~~06:00 to ~~16~~18:00 UTC. The black box denotes the RHI scan that is discussed in further detail in Section 4.1.

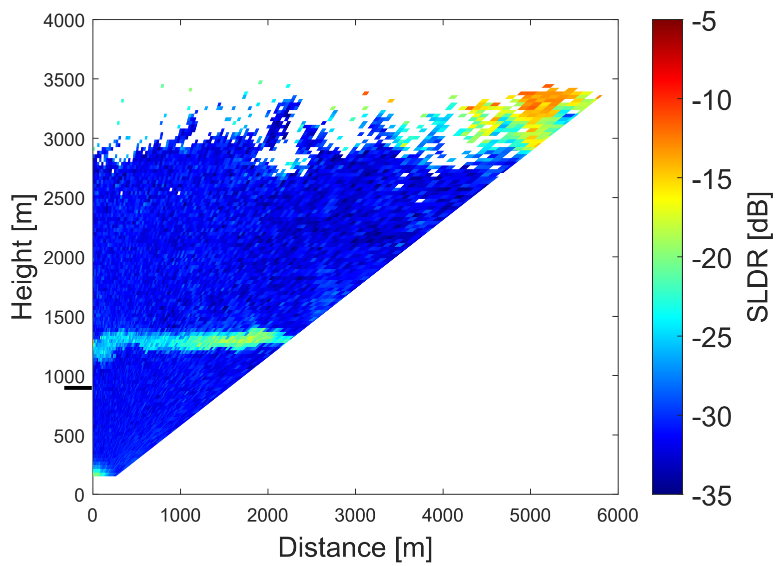

Figure 8. RHI scan of SLDR observed on 13 February 2017, at 13:31 UTC in Limassol from 90° to 150° elevation angle. The black horizontal line on the y axis mark the height of the layer analysed in Figure 9.

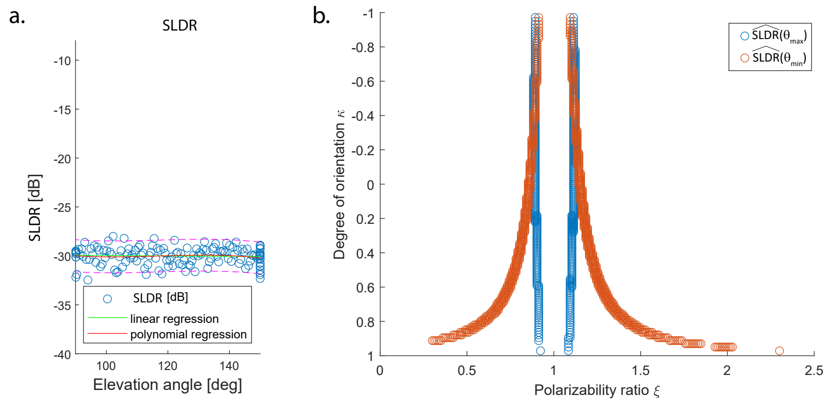

Figure 9. Detailed view into the isometric-shape case study presented in Figure 8 for the layer from 868 m to 899 m height. (a) Distribution of measured values of SLDR from θ_{min} to θ_{max} elevation angle and associated linear and polynomial fits. The dashed pink lines in (a) correspond to the 95% prediction interval from the third degrees polynomial function, used to determine the intersection of $\widehat{\mathrm{SLDR}}(\theta_{\mathrm{min}})$ and $\widehat{\mathrm{SLDR}}(\theta_{\mathrm{max}})$. (b) Intersection between $\widehat{\mathrm{SLDR}}(\theta_{\mathrm{min}})$ and $\widehat{\mathrm{SLDR}}(\theta_{\mathrm{max}})$ at θ_{min} and θ_{max}, respectively.

increasing from θ_{min} to θ_{max} where $\frac{\partial \rho_s}{\partial \theta} < lim_{\rho_s}$ $\mathrm{SLDR}(\theta_{\mathrm{min}}) < \mathrm{lim}_{\mathrm{pro}}$ and $\mathrm{SLDR}(\theta_{\mathrm{max}}) < \mathrm{lim}_{\mathrm{pro}}$ and $\frac{\partial \mathrm{SLDR}}{\partial \theta} < lim_{\mathrm{SLDR}}$. Regarding Table 2, this configuration describes the isometric primary particle shape class. Finally, the vertical distribution of ξ in the cloud is calculated following Section 3.3 and is shown in Figure 10.

RHI-scans of (a) δ_s and (b) ρ_s observed on 13 February 2017, at 13:31 UTC in Limassol from 90° to 150° elevation angle. The black horizontal lines on the y axis mark the height of the analysed layer.

Detailed view into the isometric-shape case study presented in Figure 8 for the layer from 868 m to 899 m height. (a) Distribution of measured values of δ_{s} and ρ_{s} from θ_{min} to θ_{max} elevation angle and associated linear and polynomial fits. The dashed pink line in (a) corresponds to the 95% prediction interval from the third degrees polynomial function, used to determine the intersection of $\hat{\delta}_{\mathrm{s}}(\theta_{\mathrm{min}})$ and $\hat{\delta}_{\mathrm{s}}(\theta_{\mathrm{max}})$. (b) Intersection between $\hat{\delta}_{\mathrm{s}}(\theta_{\mathrm{min}})$ and $\hat{\delta}_{\mathrm{s}}(\theta_{\mathrm{max}})$ at θ_{min} and θ_{max}, respectively.

Concerning the observations, the melting layer is well identified by a variable ξ, as explained in introduction of Section 4, in the height range from 11501250 m to 1400 mheight1350 m. Below this layer, ξ ξ takes values around 1 which describes isometric or less dense particles (Section 3.2). Looking at the Cloudnet classification (Figure 7), the drizzle-or-rain class dominates the measurement at heights below approximately 1300 m . The 1000 m height, which can be extended to the melting layer at the transition between ice and rain is recognizable by elevated and scattered values of δ_{s} in Figure 8aaround 1300 m height, taking in account the misidentified drop due to the melting layer detection of Cloudnet, as previously explained. Figure 7 shows, in the blue black box, a temperature higher than 0°C in this layer, which confirms the presence of liquid droplets, i.e., isometric particles. Application of the VDPS approach results in derivation of the same primary isometric isometric primary particle shape class as determined based on the auxiliary observations (temperature and Cloudnet classification). Above the melting layer from 1700 m to 2800 m height, the VDPS method derived isometric or less dense particles, as well. Given that

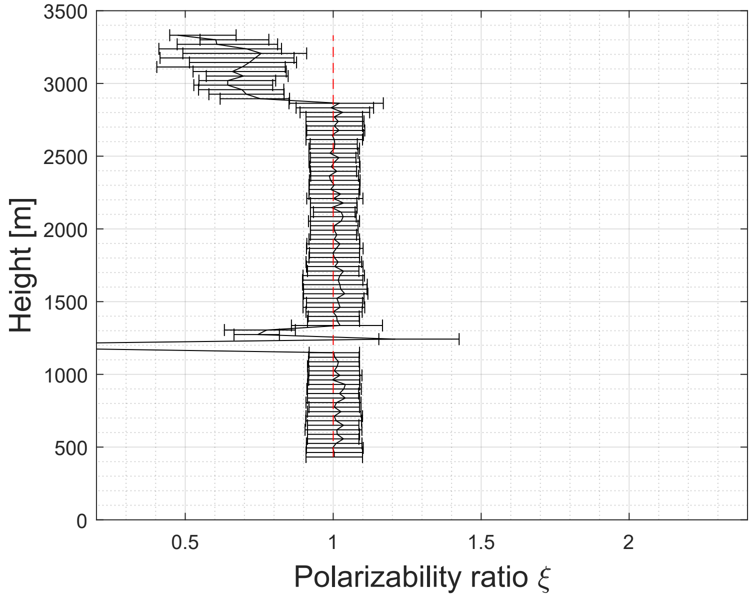

Figure 10. Vertical distribution of ξ as calculated with the VDPS method for each layer of the isometric-shape case study observed ~~at~~ in Limassol ~~,~~ on 13 February 2017, 13:31 UTC.

temperatures are below freezing level at these heights and that Cloudnet identified a mix of ice and supercooled droplets, it is likely that these isometric or less dense particles are the result of mixed-phase cloud processes, such as riming or aggregation, ~~as both of which form isometric graupel particles or aggregates, respectively~~which cannot unambiguously be identified solely with the VDPS method. Based on the VDPS method, the height level of the particle shape transition can be determined to be present at around 2800 m. Above, ξ was found to be well below 1, representing oblate particles, whose formation is also corroborated by the ambient temperatures of around $-15°\mathrm{C}$ at this height level (see Figure 7). Applicability of the VDPS method is in the present case limited with respect to the interpretation of the microphysical process which led to the formation of the layer with isometric particle shape between approximately ~~1.5 and 2.7 km~~ 1500 m and 2700 m height. Doppler spectral methods or multi-frequency approaches could help here to investigate the possible contributions of riming and aggregation (Kneifel et al., 2016; Radenz et al., 2019; Kalesse-Los et al., 2022; Vogl et al., 2022).

4.2 Prolate particle shape class: Columnar crystals on 4 January 2017 at 04:30 UTC

The second case study chosen to evaluate the VDPS method is dedicated to the characterization of columnar crystals. The corresponding measurement was recorded in Limassol on ~~4 January 2017 at 04~~8 December 2016 during an RHI scan from 00:31 to 00:33 UTC. Figure 11 presents the Cloudnet classification for the time range from 00~~to 12 UTC of 4 January 2017~~:00 to 03:00 UTC on 8 December 2016, with the selected case study marked by the ~~green~~ black frame. Figure 12 ~~a~~ shows the RHI scans of ~~δ_s and ρ_s from 04~~SLDR from 90° to 150° elevation angle at 00:31 UTC. ~~The rain event, which is shown after 0430~~

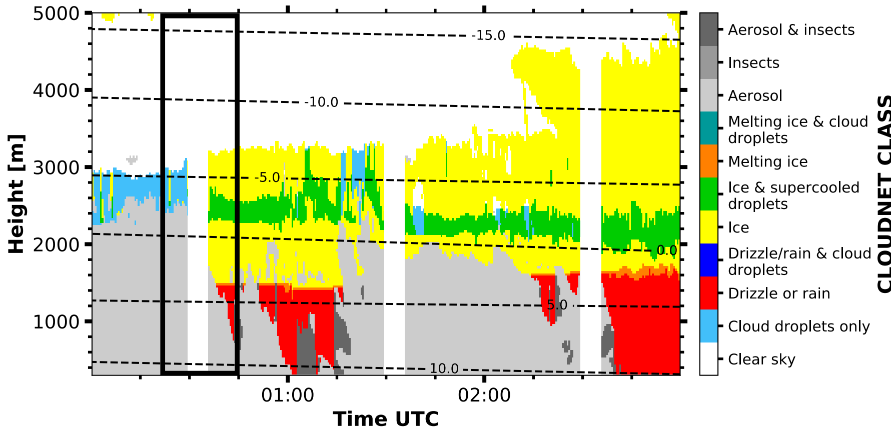

Figure 11. Cloudnet target classification mask as derived for observations at Limassol on 8 December 2016 from 00:00 to 03:00 UTC.The black box denotes the RHI scan that is discussed in further detail in Section 4.2.

UTC in Fig 11 is not yet visible in the RHI scans. In turn, the melting layer is well recognizable at around 1450 m height. This melting layer is characterized by elevated values of δ_s of around -10 dB In this RHI scan, high values of SLDR are observed at all elevation angles from $\theta_{\min}$ to $\theta_{\max}$. The onset of rain is barely visible by δ_s values which suddenly become very low (around -30 dB) below the melting layer, as is characteristic for isometric particles. Above the melting layer, the Cloudnet classification shows identified ice particles and a mixed-phase layer at around 2200 m height. Cloudnet target classification mask as derived for observations at Limassol on 4 January 2017 from 00:00 to 12:00 UTC.The green and blue boxes denote the two scans that are discussed in further detail in Sections 4.2 and 4.3, respectively.

Above the melting layer, several ice-containing layers with different elevation-angle dependencies of δ_s can be distinguished. In the layer from 1900 m to 2400 m height, δ_s is around (between -20 dB and -15 dB), suggesting that the cloud is well homogeneous and that ice particles have a high capability to depolarize the returned radar signals. According to Reinking et al. (2002) , particles having a SLDR from -20 dB to -15 dB . A second layer between 1500 m and 1900 m height is characterized by lower values of δ_s of around -20 dB. ρ_s increases from $\theta_{\min}$ to $\theta_{\max}$ while δ_s is constant. can be classified at first glance as needles or hollow columns. This constellation excludes isometric particles and oblate particles and is a specific property of columnar crystals (see Table 2). As for the first case study, the retrieval is visualized only for one specific layer, which in this case spans from 1617 2458 m to 1648 2490 m height, indicated by the black line on the y-axis in Figure 12. Figure 13a shows $\frac{\partial \delta_s}{\partial \theta}$ and $\frac{\partial \rho_s}{\partial \theta}$ calculated with the linear regression function. These gradients of δ_s and ρ_s are such as $\frac{\partial \delta_s}{\partial \theta} < lim_{\delta s}$ and $\frac{\partial \rho_s}{\partial \theta} > lim_{\rho s}$. The 95% prediction interval is the SLDR linear regression represented by the green line, which confirms that $\frac{\partial \mathrm{SLDR}}{\partial \theta} < lim_{\mathrm{SLDR}}$. The polynomial fit represented by the dashed pink line and red curve is used at $\theta_{\min}$ to $\theta_{\max}$ to calculate $\delta_s(\theta_{\min})$ and $\delta_s(\theta_{\max})$ $\mathrm{SLDR}(\theta_{\min})$ and $\mathrm{SLDR}(\theta_{\max})$, as elaborated in Section 3.2. In Figure 13b, once again two intersections of $\hat{\delta}_s(\theta_{\max})$ and $\hat{\delta}_s(\theta_{\min})$ $\widehat{\mathrm{SLDR}}(\theta_{\min})$ and $\widehat{\mathrm{SLDR}}(\theta_{\max})$ exist for this layer. Considering the positive gradient of ρ_s and

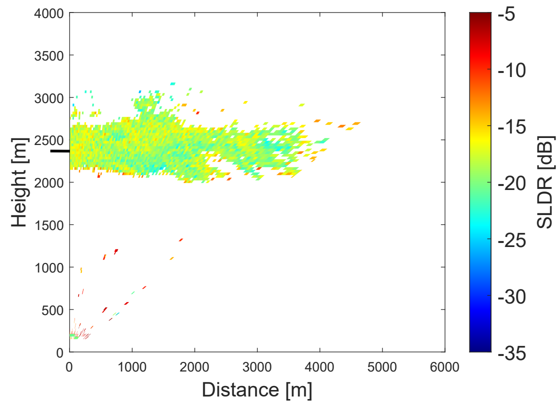

Figure 12. ~~RHI-scan~~ RHI scan of ~~(a) δ_s and (b) ρ_s~~ SLDR on ~~4 January 2017~~8 December 2016, at ~~04~~00:31 UTC~~in~~, Limassol, from 90° to 150° elevation angle. The black horizontal ~~lines~~ line on the y axis mark the height of the ~~analysed~~ layer analysed in Figure 13.

~~the constant behaviour of δ_s~~constant distribution ($\frac{\partial \mathrm{SLDR}}{\partial \theta} < lim_{\mathrm{SLDR}}$) and high values of SLDR ($\mathrm{SLDR}(\theta_{\mathrm{min}}) > \mathrm{lim}_{\mathrm{pro}}$ and $\mathrm{SLDR}(\theta_{\mathrm{max}}) > \mathrm{lim}_{\mathrm{pro}}$), we can identify the intersection in the columnar particle shape class ~~with~~ (see Table 2), resulting in $\xi > 1$ and $\kappa < -0.8$ as the ~~correct one.~~

most likely one. Figure 14 shows the vertical profile of ξ which confirms the dominance of prolate particles ~~above the melting layer. The variability of ξ over the range from 1 to 2 is generally caused by the prolate shape of columnar crystals present within this cloud. From 2400 m to 1800 m height, the presence of columnar crystals with high axis ratio and/or high density such as compact needles is likely, as ξ in this layer exceeds 1.5.~~ in the investigated cloud. Accordingly, the Cloudnet classification, shown in Figure 11 (~~green~~ black box), classifies the hydrometeors ~~as a mix of ice crystals and~~ before the RHI scan as supercooled liquid droplets~~. The melting layer is located at around 1450~~, and after the RHI scan as ice-containing and partly mixed-phase layer down to about 1500 m height~~, where the transition between liquid droplets (red) and ice crystals (yellow) is visible in Figure 11~~. A rain event occurs a few minutes after the RHI scan, defining drizzle or rain. The temperature of the investigated case ranges from ~~0°C at the melting layer level and −10°C~~ −3°C at the cloud base and −7°C at the cloud top. This temperature range is characteristic for the formation of hydrometeors in the columnar particle shape class, which demonstrates the ability of VDPS to derive prolate particles.

4.3 Oblate particle shape class: ~~Dendritic ice~~ Plate-like crystals on 4 January 2017 at 01:30 UTC

The third case study aims on the description of oblate particles, such as ~~dendritic~~ plate-like crystals. The corresponding measurement was recorded in Limassol on 4 January 2017 ~~at~~ during an RHI scan from 01:~~30~~31 to 01:33 UTC. The observed cloud system is marked by the ~~blue~~ black frame in Figure ~~11~~15. The observation was characterized by the presence of a relatively homogeneous liquid-topped ice cloud in the height range from 3200 m to 4200 m. ~~Figures 16 a and 16b show the RHI scans of δ_s and ρ_s, respectively~~Figure 16 shows the RHI scan of SLDR from 90° to 150° elevation angle at 01:31 UTC.

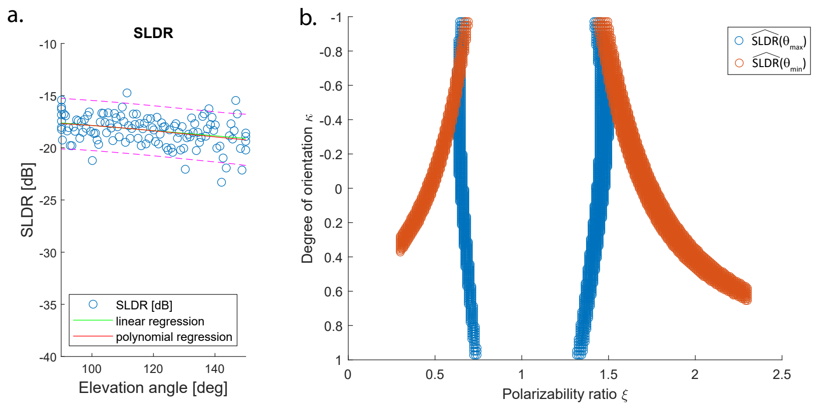

Figure 13. Detailed view into the columnar-shape case study presented in Figure 12 for the layer from ~~1617~~2458 m to ~~1648~~2490 m height. (a) Distribution of measured values of ~~δ_s and ρ_s~~ SLDR from $\theta_{\min}$ to $\theta_{\max}$ elevation angle and associated linear and polynomial fits. The dashed pink line in (a) corresponds to the 95% prediction interval from the third degrees polynomial function, used to determine the intersection of ~~$\hat{\delta}_s(\theta_{\min})$~~ $\widehat{\mathrm{SLDR}}(\theta_{\min})$ and ~~$\hat{\delta}_s(\theta_{\max})$~~ $\widehat{\mathrm{SLDR}}(\theta_{\max})$. (b) Intersection between ~~$\hat{\delta}_s(\theta_{\min})$~~ $\widehat{\mathrm{SLDR}}(\theta_{\min})$ and ~~$\hat{\delta}_s(\theta_{\max})$~~ $\widehat{\mathrm{SLDR}}(\theta_{\max})$ at $\theta_{\min}$ and $\theta_{\max}$, respectively.

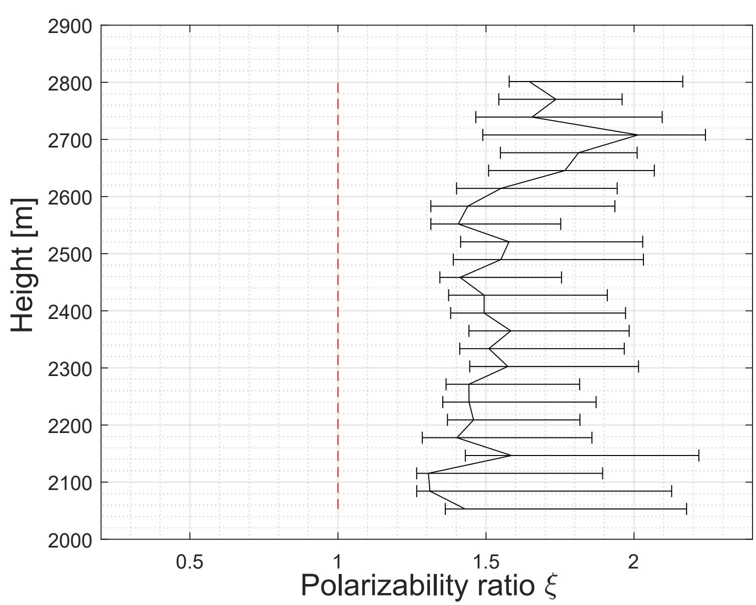

Figure 14. Polarizability ratio ξ calculated for each layer with the VDPS-method for the columnar-shape case study, observed at Limassol on ~~4 January 2017~~8 December 2016, at ~~04~~00:31 UTC.

An increase of ~~both δ_s~~ SLDR from -30 dB to -10 dB between θ_{min} and ~~ρ_s from θ_{min} to~~ θ_{max} ~~, respectively,~~ is visible. ~~These gradients are particularly visible~~ The linear regression is represented by the green line in Figure 17a which exemplarily shows the ~~layer from 3300~~retrieval for the layer from 3300 m to ~~3331~~3331 m height, represented by the black line on the y-axis in Figure 16~~, where $\frac{\partial \delta_s}{\partial \theta}$~~. In this case, $\frac{\partial \mathrm{SLDR}}{\partial \theta}$ > ~~$lim_{\delta s}$~~ lim_{SLDR}. SLDR(θ_{min}) and SLDR(θ_{max}) are calculated based on the values retrieved from the polynomial fit at θ_{min} and ~~$\frac{\partial \rho_s}{\partial \theta} > lim_{\rho s}$. ρ_s increases strongly from 90° to 110° elevation angle and levels off at 1 until~~ θ_{max}~~. $\delta_s(\theta_{\mathrm{min}})$ and $\delta_s(\theta_{\mathrm{max}})$ are calculated by as the mean of all data points contained in the 95% prediction interval of the polynomial fit represented by the dashed pink curves in Figure 17. According to Figure 5, the derived curve of ρ_s is typical of the polarimetric representation of the oblate particle class, as dendritic crystals.~~ , i.e., the red curve represented in Figure 17a. In Figure 17b, we see two intersections between ~~$\hat{\delta}_s(\theta_{\mathrm{min}})$ and $\hat{\delta}_s(\theta_{\mathrm{max}})$~~the isolines of $\widehat{\mathrm{SLDR}}(\theta_{\mathrm{min}})$ and $\widehat{\mathrm{SLDR}}(\theta_{\mathrm{max}})$. This configuration, associated with a positive ~~gradient of both polarimetric parameters δ_s and ρ_s (~~linear regression of the polarimetric parameter SLDR (see table 2), implies to select the intersection at $\xi < 1$ and $\kappa > 0.8$ for determination of the exact polarizability ratio, which corresponds to the oblate primary particle shape class. The vertical distribution of ξ presented in Figure 18 indicates $\xi < 1$ for all layers in the investigated cloud. The values of ξ ~~for this cloud is relatively constant between 0.3 and 0.5 which indicates that particles~~ are relatively constant around 0.4 from 3100 m to 3600 m height corresponding to particles which are strongly oblate and rather dense, ~~which points~~ pointing likely to the class of thick plate crystals (Reinking et al., 2002; Matrosov et al., 2012). On the other hand, above 3600 m height, $\xi \approx 0.55$ was observed, representing particles which are likely less dense such as plates or dendritic crystals. In the Cloudnet classification shown in Figure ~~11~~15, where the period of approximately 1 hour around the investigated RHI scan is indicated by the ~~blue~~ black rectangle, ice crystals and contributions of supercooled liquid droplets at cloud top ~~where~~ were identified. The temperature in the cloud ~~ranged~~ ranges from -15°C at cloud top to -10°C at cloud base. Laboratory studies suggest that, in this temperature range, the primary formation of ~~dendritic~~ plate-like ice crystals is most likely to occur (Bailey and Hallett, 2009). Hence, there is a remarkably good agreement between results of the VDPS method and observations for this case study, as well.

4.4 Microphysical transformation: case study from 2 February 2017, 13:31 UTC

By means of a final case study, the potential of the VDPS method for exploration of the vertical evolution of particle shapes from cloud top to cloud base is discussed. The corresponding measurement was recorded in Limassol on 2 January 2017. In Figure 19, the Cloudnet target classification mask of the observed cloud system is shown. The black frame in Figure 19 highlights the time period around the RHI scan at 13:31 (white vertical bar), which will be analysed below. As can be seen from the Cloudnet classification, ice crystals were identified at all heights from cloud top (around 8500 m) down to the melting layer, which was classified at a height of around 1700 m. Only at heights between around 2000–2500 m, few data points of mixed-phase conditions were identified. Also in Figure 20, which shows the 13:31 UTC RHI scan of SLDR from 90° to 150° elevation angle, the melting layer is well represented at around 1700 m height by increased values of SLDR at all elevation angles. Focusing on the height range above the melting layer, the elevation dependency of SLDR shows a distinct evolution from cloud top to bottom. At the top of the cloud, at around 8000 m height, we can observe a strong increase of SLDR from θ_{min} to θ_{max} (-30 dB at θ_{min} and -5 dB at θ_{max}). Moving away from the cloud top towards the melting layer, the increase

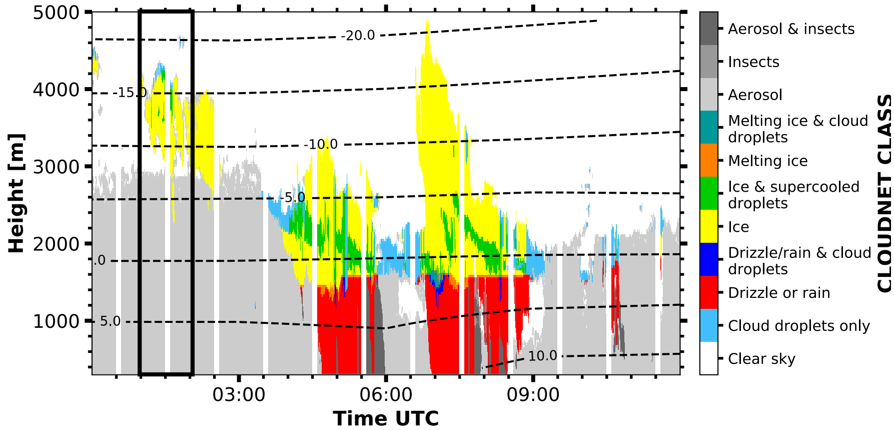

Figure 15. ~~RHI-scan of (a) δ_s and (b) ρ_s~~ Cloudnet target classification mask as derived for observations at Limassol on 4 January 2017 ~~, at 01:31 UTC in Limassol~~ from ~~90°~~ 00:00 to ~~150° elevation angle~~12:00 UTC. The black ~~horizontal lines on~~ box denotes the ~~y axis mark the height of the analysed layer~~RHI scan that is discussed in further detail in Section 4.3.

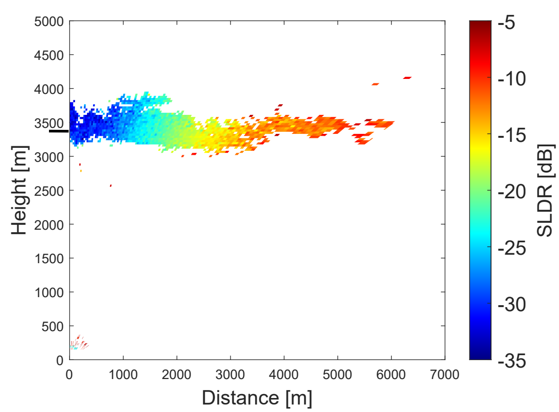

Figure 16. RHI-scan of SLDR on 4 January 2017, at 01:31 UTC in Limassol from 90° to 150° elevation angle. The black horizontal lines on the y axis mark the height of the layer analysed in Figure 17.

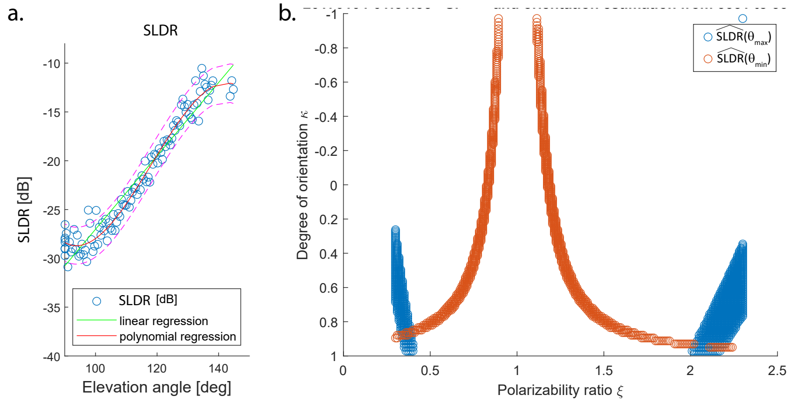

Figure 17. Detailed view into the ~~dendritic-shape~~ plate-like-shape case study presented in Figure 8 for the layer from ~~3300~~ 3300 m to ~~3331~~ 3331 m height. (a) Distribution of measured values of ~~δ_s and ρ_s~~ SLDR from $\theta_{\min}$ to $\theta_{\max}$ elevation angle and associated linear and polynomial fits. The dashed pink line in (a) corresponds to the 95% prediction interval from the third degrees polynomial function, used to determine the intersection of ~~$\hat{\delta}_s(\theta_{\min})$~~ $\widehat{\mathrm{SLDR}}(\theta_{\min})$ and ~~$\hat{\delta}_s(\theta_{\max})$~~$\widehat{\mathrm{SLDR}}(\theta_{\max})$. (b) Intersection between ~~$\hat{\delta}_s(\theta_{\min})$~~ $\widehat{\mathrm{SLDR}}(\theta_{\min})$ and ~~$\hat{\delta}_s(\theta_{\max})$~~ $\widehat{\mathrm{SLDR}}(\theta_{\max})$ at $\theta_{\min}$ and $\theta_{\max}$, respectively.

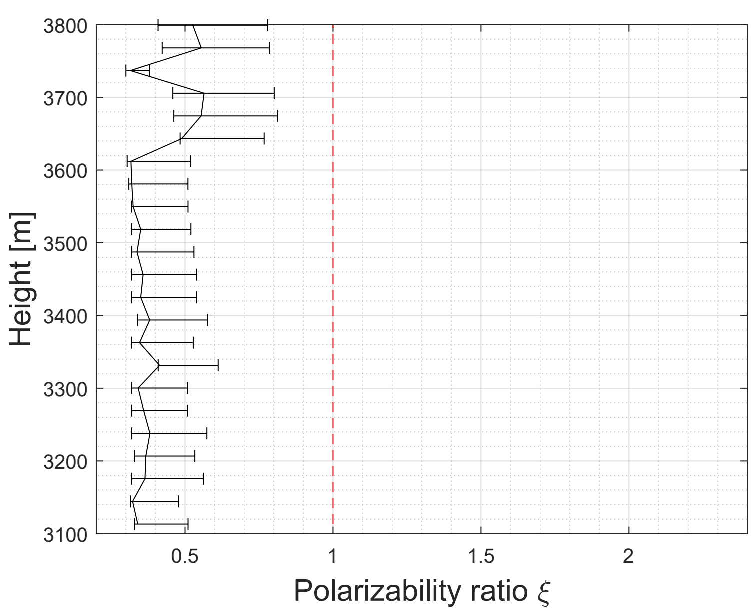

Figure 18. Polarizability ratio ξ calculated for each layer ~~calculated~~ with the ~~new~~ VDPS method for a ~~dendritic-shape~~ plate-like-shape case study observed at Limassol, on 4 January 2017, at 01:31 UTC.

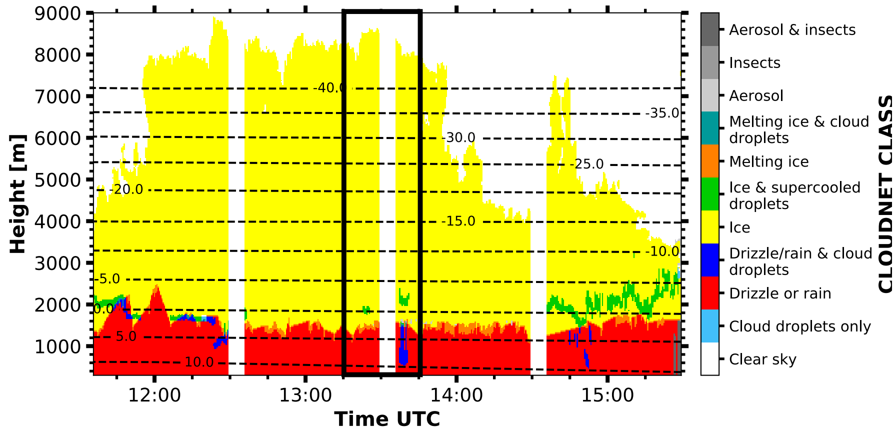

Figure 19. Cloudnet target classification mask as derived for observations at Limassol on 12 February 2017 from 11:30 to 15:30 UTC.

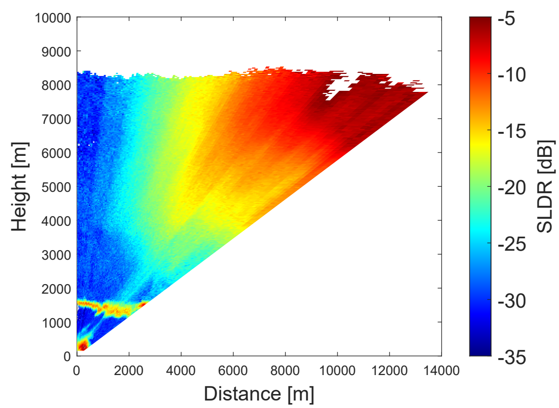

Figure 20. RHI scan of SLDR from 90° to 150° elevation angle observed in Limassol on 2 January 2017, 13:31 UTC.

of SLDR from $\theta_{\rm min}$ to $\theta_{\rm max}$ becomes gradually less pronounced. Slightly above the melting layer ($\approx$ 2000 m height), SLDR assumes values of around -30 dB at all elevation angles. The gradual change of the elevation dependency of SLDR from cloud top to cloud base translates into the vertical distribution of the polarizability ratio, as is illustrated in Figure 21. From 8000 m to 2000 m height, the polarizability ratio ξ increases gradually from 0.3, corresponding to very oblate and dense particles, such as plates, to 0.8 corresponding to less dense oblate particles such as dendrites or aggregates. Between 2000 m height and the melting layer, located at 1700 m height, the polarizability ratio ξ is close to 1 corresponding to particles with low density or generally spherical particles. This gradual increase in ξ informs about a vertical change in particle shape while the ice crystals sedimented through the cloud system. As outlined earlier, a direct determination of the the types of microphysical processes

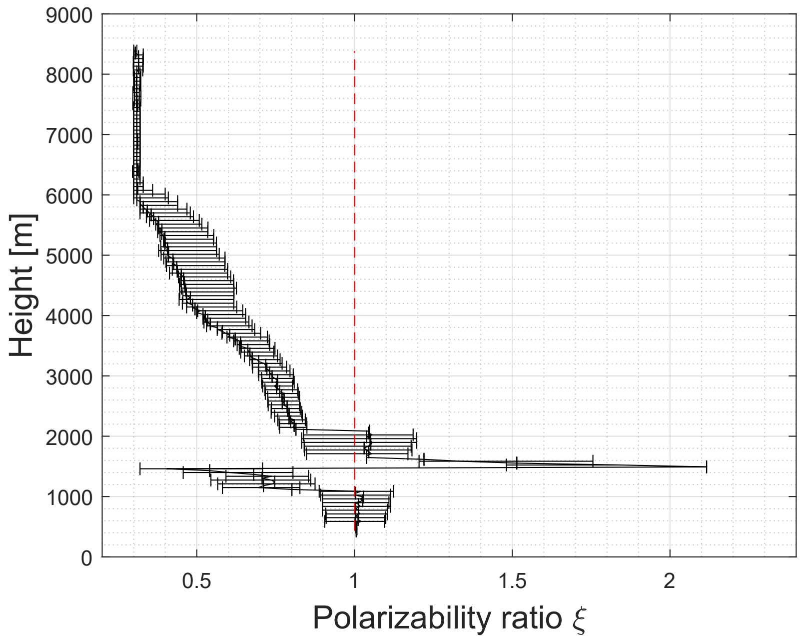

Figure 21. Profile of the polarizability ratio ξ on 2 January 2017, 13:31 UTC, Limassol, as obtained from the RHI scan of SLDR presented in Fig. 20.

that occurred in this case cannot be achieved, as further constraints must be incorporated for a thorough interpretation as is outlined in Section 5.

5 Discussion and conclusions

In this article, the Vertical-Distribution-of-Particle-Shape (VDPS) method was introduced. Based on earlier studies, which have succeeded in demonstrating the applicability of polarimetric parameters from cloud radar to estimate the particle shape (Matrosov et al., 2012; Myagkov et al., 2016a), this new approach aids one to characterize the shape of cloud particles from scanning SLDR-mode cloud radar observations. ~~The~~ The new VDPS method is based only on a single polarimetric parameter - SLDR. Another novelty of the VDPS method is the idea that a profile of the polarizability ratio can be used not only to derive shape of pristine ice crystals at cloud tops (as done in Myagkov et al. (2016a, b)) but also as an indicator of microphysical processes affecting particle shape and/or apparent density in deep precipitating clouds. In addition, the VDPS method is more versatile than the original approach of Myagkov et al. (2016a), which was developed for hybrid-mode cloud radars, requiring a complex calibration of ZDR and correlation coefficient. We will compare the two methods in an upcoming campaign in Switzerland (winter 2023/24), where an SLDR (Metek S/N MBR5) and a hybrid-mode radar (Metek S/N MBR7) will operate co-located next to each other.

The 45°-slanted linear depolarization (SLDR) mode was specifically chosen for the purpose of minimizing the influence of ~~particle orientation by~~ fluctuations in the particle orientation during sedimentation, called wobbling effect (Matrosov et al., 2001), while providing well suited and relatively ~~easily~~ easy observable input parameters for the shape retrieval. The VDPS approach represents a new, versatile way to study microphysical processes by combining a spheroidal scattering model (Myagkov et al., 2016b) applied only to ~~$\hat{\delta}_{\mathrm{s}}$, with real measurements of δ_{s} and ρ_{s}~~ $\widehat{\mathrm{SLDR}}$. In this paper, the VDPS method was introduced and validated by means of case studies collected in the frame of the CyCARE field campaign (Limassol, Cyprus), for three representative shape classes ~~,~~ oblate, isometric and prolate particles, which ~~present a polarizability ratio $\xi < 1$, $\xi = 1$ and $\xi > 1$~~ are characterized by polarizability ratios of $\xi < 1$, $\xi = 1$ and $\xi > 1$, respectively. ~~Before validating~~ A fourth case study demonstrated the applicability of the VDPS method for evaluation of the evolution of the ice crystal shape between top and base of a deep cloud system. Before validation of the VDPS method, the algorithm was tested and calibrated with success based on observational datasets from two field campaigns, CyCARE in Limassol, Cyprus, and DACAPO-PESO in Punta Arenas, Chile (Radenz et al., 2021), which sums up to three years of SLDR measurements at two different places.

The vertical distribution of the polarizability ratio ξ is precious because it informs about the transformation ~~, sedimentation or stratification of hydrometeors in a~~ of apparent particle shape or density in an investigated cloud from top to bottom, which shows that microphysical processes are occurring. Based on the information about the vertical distribution of particle shape in a cloud, the VDPS method provides valuable constraints for microphysical fingerprinting studies (Section 4.4). The height-resolved view of the vertical distribution and evolution of particle shape in a cloud is helpful to study and characterize mixed-phase cloud processes in the onset phase of precipitation. While isometric, columnar and oblate particle shapes can well be distinguished with the VDPS method, discrimination between graupel (formed by riming) and aggregates (formed by aggregation) remains a challenge and is currently not possible solely with ~~this~~ the VDPS method. Nevertheless, both processes can ~~be identified~~ potentially be inferred based on the vertical evolution of ξ between cloud top and cloud base. In future, we therefore plan to associate the VDPS method with Doppler spectral methods in order to detect supercooled liquid droplets in mixed-phase clouds and to estimate the fall velocity of particles, which ~~are relevant information to discriminate riming from aggregation~~ provide relevant constraints for the discrimination between riming and aggregation processes. Indeed, riming processes require the presence of supercooled liquid droplets and the formed graupel are falling faster than aggregates because of their higher density (Kneifel et al., 2016; Vogl et al., 2022).

~~The VDPS method was implemented by means of an automatized framework, which permits us to obtain statistics about the particle shape for a long period of measurements and covering several field campaigns.~~ Besides the mentioned strengths of the VDPS method, there are also certain limitations, which can eventually be overcome in future development steps. The first one is corresponding to the radar antenna quality, as it determines the ~~calibration of δ_{s} and ρ_{s}~~ calibration of SLDR. ~~Polarimetric parameters δ_{s} and ρ_{s} are~~ The polarimetric parameter SLDR is intrinsically dependent on the calibration of the antenna and the differential phase of the transceiver unit. Care must be taken to ensure a good calibration of the radar system. ~~However, as was shown in this study, qualitative information about the elevation dependency of ρ_{s} is sufficient to identify the primary particle shape class when assuming horizontally oriented hydrometeors. For determination of the degree of orientation, the calibration of ρ_{s} needs to be improved so that it can be used quantitatively. In~~ A good co-cross channel isolation should be aspired in order to obtain highest accuracy of the retrieval, especially for values of ξ that are close to 1. Secondly, in its current development state, the VDPS method is also only capable to investigate the shape of the hydrometeor population that determines the main peak of the co-channel Doppler spectrum, as characterized by the highest peak of each Doppler spectrum obtained during an RHI scan at any given height level. However, a new approach taking into account the comparison between main peaks detected in the co- and cross-channels can give more information about the ice crystal populations in a volume: if the main peaks are similar in the co- and cross-channels, it means that the main hydrometeor population depolarizes the most. On the other hand, the presence of different main peaks in the co- and cross-polarized Doppler spectra would imply the presence of a second hydrometeor population which depolarizes strongly, while still a non-polarizing hydrometeor population dominates the co-channel signal.

The technique can currently thus not be used for evaluating the RHI scans for coexistence of several particle populations, as they might be superimposed by means of their differential fall velocities collected in a Doppler spectrum. Such peak separation techniques have already been developed for vertically pointing cloud radar measurements (Kalesse et al., 2019; Radenz et al., 2019) and ~~will~~ can potentially be adapted for scanning cloud radars in the near future.

~~Finally, our investigations have shown that applicability of the VDPS method is given even when measurements of δ_s are obtained only at two elevation angles θ_{min} and θ_{max}, which permits to change the duration of the required RHI scans as measurements at intermediate angles are not required any more, in contrast to~~ Overall, the ~~original approach of Myagkov et al. (2016b). This will considerably shorten the required amount of measurement time for each shape-retrieval measurement and improve the resolution of data points~~VDPS technique has the potential to become a standard procedure in the analysis of long-term observations from scanning SLDR cloud radar systems. Given the broad availability of scanning LDR-mode cloud radars in Europe, the VDPS method provides good reasoning to update these to SLDR mode with low effort and investment.

Code and data availability. The cloud-radar raw data and retrieval codes are available upon request. Please contact the first or second author. Cloudnet data are available at https://cloudnet.fmi.fi. For plotting of the data, the tool pyLARDA, available at https://github.com/lacros-tropos/larda, was used.

Author contributions. AT developed the VDPS method, analysed the data and drafted the manuscript supervised by PS. JB conducted the CyCARE campaign and operated LACROS. PS, MR, and JB generated the Cloudnet datasets and supervised the data processing chain. AM suppored me during the starting phase of the development work on the VDPS method and developed the spheroidal scattering model.

Competing interests. The contact author has declared that neither they nor their co-authors have any competing interests.

Acknowledgements. Development of the VDPS method was funded by the Deutsche Forschungsgemeinschaft (DFG – German Research Foundation) project PICNICC (SE2464/1-1 and KA4162/2-1). The authors wish to thank Cyprus University of Technology, Limassol, Cyprus, for their logistic and infrastructural support during the LACROS deployment. We gratefully acknowledge the ACTRIS Cloud Remote Sensing Unit for making the Cloudnet datasets publicly available. LACROS operations were supported by the European Union (EU) Horizon 2020 (ACTRIS; grant no. 654109) and the Seventh Framework Programme (BACCHUS; grant no. 603445). The authors also wish to thank Metek GmbH, Elmshorn, for the technical support related to the Mira-35 radar.

References

Ansmann, A., Mamouri, R.-E., Hofer, J., Baars, H., Althausen, D., and Abdullaev, S. F.: Dust mass, cloud condensation nuclei, and ice-nucleating particle profiling with polarization lidar: updated POLIPHON conversion factors from global AERONET analysis, Atmospheric Measurement Techniques, 12, 4849–4865, https://doi.org/10.5194/amt-12-4849-2019, 2019.

Avramov, A. and Harrington, J. Y.: Influence of parameterized ice habit on simulated mixed phase Arctic clouds, Journal of Geophysical Research: Atmospheres, 115, https://doi.org/https://doi.org/10.1029/2009JD012108, 2010.

Bailey, M. P. and Hallett, J.: A Comprehensive Habit Diagram for Atmospheric Ice Crystals: Confirmation from the Laboratory, AIRS II, and Other Field Studies, Journal of the Atmospheric Sciences, 66, 2888 – 2899, https://doi.org/10.1175/2009JAS2883.1, 2009.

Bringi, V. and Chandrasekar, V.: Polarimetric Doppler Weather Radar: Principles and Applications, https://doi.org/10.1017/CBO9780511541094, 2001.

Bühl, J., Seifert, P., Myagkov, A., and Ansmann, A.: Measuring ice- and liquid-water properties in mixed-phase cloud layers at the Leipzig Cloudnet station, Atmospheric Chemistry and Physics, 16, 10 609–10 620, https://doi.org/10.5194/acp-16-10609-2016, 2016.

Bühl, J., Seifert, P., Radenz, M., Baars, H., and Ansmann, A.: Ice crystal number concentration from lidar, cloud radar and radar wind profiler measurements, Atmospheric Measurement Techniques, 12, 6601–6617, https://doi.org/10.5194/amt-12-6601-2019, 2019.

Chandrasekar, V. and Keeler, R. J.: Antenna Pattern Analysis and Measurements for Multiparameter Radars, Journal of Atmospheric and Oceanic Technology, 10, 674 – 683, https://doi.org/10.1175/1520-0426(1993)010<0674:APAAMF>2.0.CO;2, 1993.

Fan, J., Han, B., Varble, A., Morrison, H., North, K., Kollias, P., Chen, B., Dong, X., Giangrande, S. E., Khain, A., Lin, Y., Mansell, E., Milbrandt, J. A., Stenz, R., Thompson, G., and Wang, Y.: Cloud-resolving model intercomparison of an MC3E squall line case, Journal of Geophysical Research: Atmospheres, 122, 9351–9378, https://doi.org/https://doi.org/10.1002/2017JD026622, 2017.

Fukuta, N. and Takahashi, T.: The Growth of Atmospheric Ice Crystals: A Summary of Findings in Vertical Supercooled Cloud Tunnel Studies, Journal of the Atmospheric Sciences, 56, 1963 – 1979, https://doi.org/10.1175/1520-0469(1999)056<1963:TGOAIC>2.0.CO;2, 1999.

Görsdorf, U., Lehmann, V., Bauer-Pfundstein, M., Peters, G., Vavriv, D., Vinogradov, V., and Volkov, V.: A 35-GHz Polarimetric Doppler Radar for Long-Term Observations of Cloud Parameters Description of System and Data Processing, Journal of Atmospheric and Oceanic Technology, 32, 675 – 690, https://doi.org/10.1175/JTECH-D-14-00066.1, 2015.

Illingworth, A. J., Hogan, R. J., O'Connor, E., Bouniol, D., Brooks, M. E., Delanoé, J., Donovan, D. P., Eastment, J. D., Gaussiat, N., Goddard, J. W. F., Haeffelin, M., Baltink, H. K., Krasnov, O. A., Pelon, J., Piriou, J.-M., Protat, A., Russchenberg, H. W. J., Seifert, A., Tompkins, A. M., van Zadelhoff, G.-J., Vinit, F., Willén, U., Wilson, D. R., and Wrench, C. L.: Cloudnet: Continuous Evaluation of Cloud Profiles in Seven Operational Models Using Ground-Based Observations, Bulletin of the American Meteorological Society, 88, 883 – 898, https://doi.org/10.1175/BAMS-88-6-883, 2007.

Kalesse, H., Vogl, T., Paduraru, C., and Luke, E.: Development and validation of a supervised machine learning radar Doppler spectra peak-finding algorithm, Atmospheric Measurement Techniques, 12, 4591–4617, https://doi.org/10.5194/amt-12-4591-2019, 2019.

Kalesse-Los, H., Schimmel, W., Luke, E., and Seifert, P.: Evaluating cloud liquid detection against Cloudnet using cloud radar Doppler spectra in a pre-trained artificial neural network, Atmospheric Measurement Techniques, 15, 279–295, https://doi.org/10.5194/amt-15-279-2022, 2022.

Kneifel, S., Kollias, P., Battaglia, A., Leinonen, J., Maahn, M., Kalesse, H., and Tridon, F.: First observations of triple-frequency radar Doppler spectra in snowfall: Interpretation and applications, Geophysical Research Letters, 43, 2225–2233, https://doi.org/https://doi.org/10.1002/2015GL067618, 2016.

Korolev, A., Mcfarquhar, G., Field, P., Franklin, C., Lawson, P., Wang, Z., Williams, E., Abel, S., Axisa, D., Borrmann, S., Crosier, J., Fugal, J., Krämer, M., Lohmann, U., Schlenczek, O., and Wendisch, M.: Mixed-Phase Clouds: Progress and Challenges, Meteorological Monographs, 58, 5.1–5.50, https://doi.org/10.1175/AMSMONOGRAPHS-D-17-0001.1, 2017.

Luke, E. P., Yang, F., Kollias, P., Vogelmann, A. M., and Maahn, M.: New insights into ice multiplication using remote-sensing observations of slightly supercooled mixed-phase clouds in the Arctic, Proceedings of the National Academy of Sciences, 118, e2021387 118, https://doi.org/10.1073/pnas.2021387118, 2021.

Löhnert, U., Schween, J. H., Acquistapace, C., Ebell, K., Maahn, M., Barrera-Verdejo, M., Hirsikko, A., Bohn, B., Knaps, A., O'Connor, E., Simmer, C., Wahner, A., and Crewell, S.: JOYCE: Jülich Observatory for Cloud Evolution, Bulletin of the American Meteorological Society, 96, 1157 – 1174, https://doi.org/https://doi.org/10.1175/BAMS-D-14-00105.1, 2015.

Madonna, F., Amodeo, A., D'Amico, G., and Pappalardo, G.: A study on the use of radar and lidar for characterizing ultragiant aerosol, Journal of Geophysical Research: Atmospheres, 118, 10,056–10,071, https://doi.org/https://doi.org/10.1002/jgrd.50789, 2013.

Matrosov, S., Mace, G., Marchand, R., Shupe, M., Hallar, A., and McCubbin, I.: Observations of Ice Crystal Habits with a Scanning Polarimetric W-Band Radar at Slant Linear Depolarization Ratio Mode, Journal of Atmospheric and Oceanic Technology, 29, 989–1008, https://doi.org/10.1175/JTECH-D-11-00131.1, 2012.

Matrosov, S. Y.: Prospects for the measurement of ice cloud particle shape and orientation with elliptically polarized radar signals, Radio Science, 26, 847–856, https://doi.org/https://doi.org/10.1029/91RS00965, 1991.

Matrosov, S. Y., Reinking, R. F., Kropfli, R. A., Martner, B. E., and Bartram, B. W.: On the Use of Radar Depolarization Ratios for Estimating Shapes of Ice Hydrometeors in Winter Clouds, Journal of Applied Meteorology, 40, 479 – 490, https://doi.org/10.1175/1520-0450(2001)040<0479:OTUORD>2.0.CO;2, 2001.

Matrosov, S. Y., Reinking, R. F., and Djalalova, I. V.: Inferring Fall Attitudes of Pristine Dendritic Crystals from Polarimetric Radar Data, Journal of the Atmospheric Sciences, 62, 241 – 250, https://doi.org/https://doi.org/10.1175/JAS-3356.1, 2005.

Morrison, H., de Boer, G., Feingold, G., Harrington, J., Shupe, M. D., and Sulia, K.: Resilience of persistent Arctic mixed-phase clouds, Nature Geoscience, 5, 11–17, https://doi.org/10.1038/ngeo1332, 2012.

Myagkov, A., Seifert, P., Wandinger, U., Bauer-Pfundstein, M., and Matrosov, S. Y.: Effects of Antenna Patterns on Cloud Radar Polarimetric Measurements, Journal of Atmospheric and Oceanic Technology, 32, 1813–1828, https://doi.org/10.1175/JTECH-D-15-0045.1, 2015.

Myagkov, A., Seifert, P., Bauer-Pfundstein, M., and Wandinger, U.: Cloud radar with hybrid mode towards estimation of shape and orientation of ice crystals, Atmospheric Measurement Techniques, 9, 469–489, https://doi.org/10.5194/amt-9-469-2016, 2016a.

Myagkov, A., Seifert, P., Wandinger, U., Bühl, J., and Engelmann, R.: Relationship between temperature and apparent shape of pristine ice crystals derived from polarimetric cloud radar observations during the ACCEPT campaign, Atmospheric Measurement Techniques, 9, 3739–3754, https://doi.org/10.5194/amt-9-3739-2016, 2016b.

Pruppacher, H. and Klett, J.: Microphysics of Clouds and Precipitation., Springer Dordrecht, https://doi.org/https://doi.org/10.1007/978-0-306-48100-0, 1997.

Radenz, M., Bühl, J., Seifert, P., Griesche, H., and Engelmann, R.: peakTree: a framework for structure-preserving radar Doppler spectra analysis, Atmospheric Measurement Techniques, 12, 4813–4828, https://doi.org/10.5194/amt-12-4813-2019, 2019.

Radenz, M., Bühl, J., Seifert, P., Baars, H., Engelmann, R., Barja González, B., Mamouri, R.-E., Zamorano, F., and Ansmann, A.: Hemispheric contrasts in ice formation in stratiform mixed-phase clouds: Disentangling the role of aerosol and dynamics with ground-based remote sensing, Atmospheric Chemistry and Physics Discussions, 2021, 1–34, https://doi.org/10.5194/acp-2021-360, 2021.

Reinking, R. F., Matrosov, S. Y., Kropfli, R. A., and Bartram, B. W.: Evaluation of a 45° Slant Quasi-Linear Radar Polarization State for Distinguishing Drizzle Droplets, Pristine Ice Crystals, and Less Regular Ice Particles, Journal of Atmospheric and Oceanic Technology, 19, 296 – 321, https://doi.org/https://doi.org/10.1175/1520-0426-19.3.296, 2002.

Ryzhkov, A. V.: Interpretation of Polarimetric Radar Covariance Matrix for Meteorological Scatterers: Theoretical Analysis, Journal of Atmospheric and Oceanic Technology, 18, 315 – 328, https://doi.org/10.1175/1520-0426(2001)018<0315:IOPRCM>2.0.CO;2, 2001.

Schimmel, W., Kalesse-Los, H., Maahn, M., Vogl, T., Foth, A., Garfias, P. S., and Seifert, P.: Identifying cloud droplets beyond lidar attenuation from vertically pointing cloud radar observations using artificial neural networks, Atmospheric Measurement Techniques, 15, 5343–5366, https://doi.org/10.5194/amt-15-5343-2022, 2022.

Solomon, A., de Boer, G., Creamean, J. M., McComiskey, A., Shupe, M. D., Maahn, M., and Cox, C.: The relative impact of cloud condensation nuclei and ice nucleating particle concentrations on phase partitioning in Arctic mixed-phase stratocumulus clouds, Atmospheric Chemistry and Physics, 18, 17 047–17 059, https://doi.org/10.5194/acp-18-17047-2018, 2018.

Tetoni, E., Ewald, F., Hagen, M., Köcher, G., Zinner, T., and Groß, S.: Retrievals of ice microphysical properties using dual-wavelength polarimetric radar observations during stratiform precipitation events, Atmospheric Measurement Techniques, 15, 3969–3999, https://doi.org/10.5194/amt-15-3969-2022, 2022.

Vogl, T., Maahn, M., Kneifel, S., Schimmel, W., Moisseev, D., and Kalesse-Los, H.: Using artificial neural networks to predict riming from Doppler cloud radar observations, Atmospheric Measurement Techniques, 15, 365–381, https://doi.org/10.5194/amt-15-365-2022, 2022.